On the role of charge transfer excitations in non-fullerene acceptors for organic photovoltaics

Samuele Giannini [a,1,]*, Daniel J.C. Sowood [b], Jesús Cerdá [a], Siebe Frederix [c], Jeannine Grüne [d], Giacomo Londi [a,2], Thomas Marsh [b], Pratyush Ghosh [b], Ivan Duchemin [f], Neil C. Greenham [b], Koen Vandewal [c], Gabriele D'Avino [e], Alexander J. Gillett [b,3,]*, David Beljonne [a,]*

[a] Laboratory for Chemistry of Novel Materials, University of Mons, Mons 7000, Belgium
[b] Cavendish Laboratory, University of Cambridge, JJ Thomson Avenue, Cambridge CB3 0HE, UK
[c] Instituut voor Materiaalonderzoek (IMO-IMOMEC), Hasselt University, Diepenbeek, Belgium
[d] Julius Maximilian University of Würzburg Am Hubland, Würzburg, 97074 Würzburg, Germany
[e] Grenoble Alpes University, CNRS, Grenoble INP, Institut Néel, 38042 Grenoble, France
[f] Grenoble Alpes University, CEA, IRIG-MEM-L_Sim, 38054 Grenoble, France

Through the development of new non-fullerene electron acceptor (NFA) materials, such as Y6 and its molecular derivatives, the power conversion efficiencies of organic photovoltaics (OPVs) have now exceeded 19 %. However, despite this rapid progress, our fundamental understanding of the unique optical and electronic properties of these Y-series NFAs is lacking, and this currently limits progress in material design. In this work, we provide a detailed computational-experimental characterisation of the archetypal NFA, Y6. To explain the significant broadening and red shift of the absorption spectrum observed when moving from the solution phase to the solid state, we first rule out more typical causes, such as J-aggregation. Instead, by considering the role of charge transfer (CT) excitations and their mixing with Frenkel exciton (FE) states, we can computationally reproduce the experimental absorption spectra of Y6 with excellent accuracy. Using transient absorption spectroscopy, we provide evidence for this dense manifold of FE-CT hybrid electronic excitations in Y6 through the prominent sub-picosecond relaxation events following supra band gap excitation. Furthermore, through sub band gap excitation, we also find states with polaronic character in Y6 that are in a dynamic equilibrium with the FE-CT hybrid states. Magnetic resonance spectroscopies reveal that these polaronic states are polaron pairs, most likely located on neighbouring Y6 molecules, not free charge carriers, as has been previously suggested. Thus, this new understanding of how the solid-state packing motif directly controls the optical and electronic properties of Y-series NFAs opens the door to intelligently design NFA materials to further increase OPV performance.

Keywords: Non-fullerene acceptors; Hybrid Frenkel-exciton/charge transfer states; Polaron pairs; Organic solar cells

---

* Corresponding authors.
E-mail addresses: Giannini, S. (samuele.giannini@cnr.it), Gillett, A.J. (alexander.gillett@liu.se), Beljonne, D. (david.beljonne@umons.ac.be).

[1] Present address: Institute of Chemistry of OrganoMetallic Compounds, National Research Council (ICCOM-CNR), I-56124 Pisa, Italy.

[2] Present address: Dipartimento di Chimica e Chimica Industriale, Universitá di Pisa, 56124 Pisa, Italy.

[3] present address: Department of Physics, Chemistry and Biology (IFM), Linköping University, 581 83 Linköping, Sweden.

https://doi.org/10.1016/j.mattod.2024.09.009

Introduction

Significant progress has been achieved in the field of organic photovoltaics (OPVs) due to extensive synthetic work, and this has now resulted in record-breaking power conversion efficiencies exceeding 19 % [1,2]. A particular family of molecular non-fullerene acceptors (NFAs), *i.e.*, Y6 and its analogues, has dominated the field since 2019 [3,4] and has been central to the recent efficiency developments [5,6]. However, despite the major performance advances enabled by Y-series NFAs, the fundamental photophysics of Y6 and its molecular derivatives is still not well understood and there is considerable debate in several areas of great relevance for OPV operation [7–10]. For example, there is no consensus yet on the reason for the significant red shift and broadening of the Y6 absorption spectrum when moving from solution to thin-film [8,10], nor on whether Y6 can spontaneously generate free charge carriers in the bulk acceptor phase [7,9,11,12]. Therefore, gaining a fundamental understanding of the optical properties and establishing structure-photophysical property relationships would provide valuable insights for knowledge-driven progress, ultimately pushing the efficiency of these materials beyond the 20 % milestone.

What makes the Y-series NFAs so special? Unlike previous generations of NFAs, materials belonging to the Y-series are based on a general A–DA′D–A structure (A = acceptor moiety, D = donor moiety). The A′ unit leads to a centrosymmetry loss relative to the previous A–D–A NFAs and the formation of a permanent dipole moment that encourages dimer formation in the crystal structure. However, the performance of OPVs is not solely determined by the chemical building blocks themselves but is also highly sensitive to the arrangement and orientation of the individual molecules in the solid-state [13]. For instance, it has been shown that, compared to earlier NFA molecular families (such as ITIC or IEICO), Y6 assembles into a unique 3D interpenetrated lattice. This structure, of which variations are common to other Y-series derivatives, shows a large number of directional face-on stackings yielding an inter-connected transport network with sizable charge and excitonic interactions [14]. Importantly, this characteristic molecular crystal packing is essentially retained in thin-film phases after processing [15–17]. This local microstructure dictates the nature of the relevant photoexcitations in both the bulk phase of the acceptor component and at the heterojunction with a donor component, with a possible mixing between localized Frenkel exciton (FE) and charge transfer (CT) excitations and a degree of wavefunction delocalization that is limited by (static and dynamic) energetic disorder [18,19]. These characteristics in turn define the optical properties and excited-state dynamics in these systems. For instance, a remarkable feature of Y6 is the dramatic change in position and shape of its spectral features upon aggregation. Specifically, worth noting is the unusually strong spectral red-shift (by ∼0.2 eV) and increased broadening when going from Y6 solution to the thin-film phase.

Curiously, recent experimental work has shown that neat Y6 can work reasonably well as a single component solar cell, with a power conversion efficiency of ∼4.5 % [11]. However, open questions still remain about whether Y6 crystalline domains are intrinsically generating a significant quantity of free charge carriers, or whether charge separation is happening at the interfaces with the electron and hole transporting layers of these 'single component' devices (potentially assisted by the electric field applied across the OPV device under operation') [20], with the device in-effect operating as a bilayer OPV. Spectroscopic and theoretical investigations on this topic point to the presence of closely interacting molecules that can yield the formation of charge transfer/separated states as precursors for possible free carrier generation [7–10]. Wang et al. were the first to infer the existence of a delocalised excited state, which they called an ‘intra-moiety state’, from transient absorption spectroscopy (TAS) measurements on neat Y6 films as well as PM6:Y6 bulk heterojunction (BHJ) blends [9]. With selective photoexcitation of Y6 in the BHJ blend, they showed that this state is an intermediate on the pathway of hole transfer to the polymer. While the exact nature of the delocalised state was not explicitly defined, it exhibited characteristics suggestive of electron-hole separation resembling that of a polaron-pair-type state. They also assigned a photo-induced absorption (PIA) feature in their TAS spectrum of a neat Y6 film at 1550 nm to this state, which was absent in solution measurements of Y6. Building on Wang et al.’s work, Price et al. made an eye-catching claim about the spontaneous generation of free charges with a 60–90 % yield in neat Y6 films [7]. This observation was based primarily on intensity-dependent external photoluminescence quantum efficiency (PLQE) measurements, where an increase in PLQE with fluence was attributed to radiative, non-geminate recombination of intrinsically generated free charges. However, it is difficult to reconcile the formation of truly ‘free’ charge carriers (*i.e.*, exceeding the Coulomb capture radius, typically of ∼5 nm in organic semiconductors [21]), with the widely reported excited state lifetime of a few hundred picoseconds in neat Y6 films, as measured by TAS [9]. Though, it is also worth noting that transient PL studies point to a longer fluorescence lifetime on the order of one nanosecond in neat Y6 films [22,23]. Thus, there is clearly significant confusion surrounding the excited state dynamics of Y6 and related molecular derivatives that needs to be addressed.

In this work, we investigate the role played by CT excitations within the bulk NFA phase in the photophysics of Y6 (Fig. 1a, b). Using state-of-the-art modelling combining high-quality electronic structure calculations [24–26], polarizable molecular embedding [27–29] and a Frenkel-Holstein-like exciton Hamiltonian [30–32], we show that the optical absorption of Y6 films is indeed largely perturbed by intermolecular interactions. We also computationally address the nature of the electronic excitations in neat Y6 films, specifically on the role and interplay between FE and CT excitations. Using TAS and magnetic resonance spectroscopy, we corroborate the findings of the quantum-chemical calculations and investigate the potential for polaronic states to form in neat Y6 films. We reveal that these polaron pair states are most probably located on neighbouring Y6 molecules and propose that they are not free charge carriers as previously suggested.

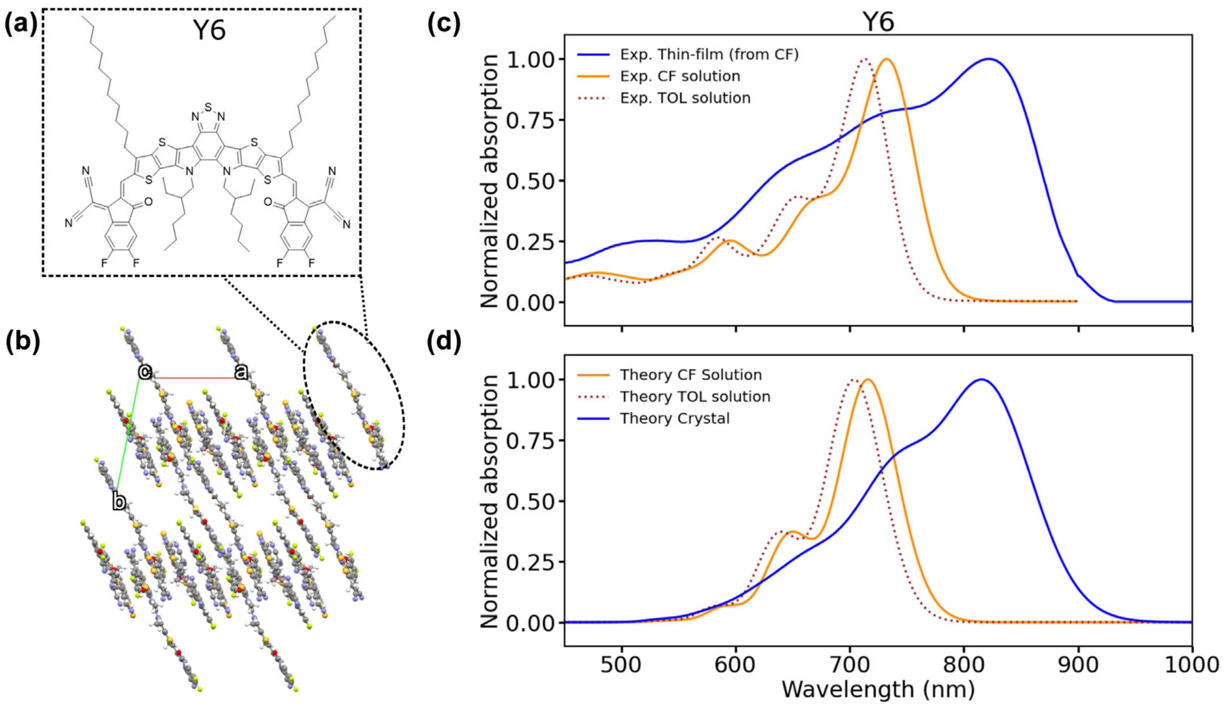

FIG. 1

(a) Molecular and (b) single-crystal structures of Y6, respectively. The alkyl side chains have been removed for clarity in the crystal structure representation. The unit cell axes a and b are shown in red and lime, respectively (axis c is eclipsed by the other two). (c) Experimental absorption spectra of Y6 in TOL (dashed brown line) and CF solution (solid orange line). CF-processed thin-film spectra obtained applying the correction for interference effects using the transfer matrix method (TMM) as described in the text. (d) Computed normalized absorption spectra of Y6 measured in TOL (dashed brown line) and CF (solid orange line). The energies of the $S_0 \rightarrow S_1$ were obtained from BSE/PCM calculations and the vibronic progressions calculated as described in Methods. The spectrum of Y6 crystal is reported with solid blue line obtained using the Frenkel-Holstein excitonic Hamiltonian (Eq. (1)) parameterized using ab-initio data as described in the text. A homogeneous spectral broadening of 60 meV was added to all computed spectra for the best comparison with experiments. No shift is applied to the computed spectra, the peak positions is determined computationally as described in the text.

Results and discussion

Y6 steady-state experimental absorption

To aid comprehension of the results, we shall first define the terminology used in the text surrounding electronic excitations with charge transfer character. In this context, we will discuss two types of charge transfer excitations that play important and distinct roles in the photophysics of Y6. The first are charge transfer states formed between neighbouring Y6 molecules in the crystalline packing motif that lie above the lowest energy Frenkel exciton transition of Y6: these will be referred to as ‘CT states’. Though not directly populated, these CT states have the potential to hybridise with the Frenkel exciton states in Y6, forming mixed character Frenkel exciton-CT (FE-CT) hybrid states (*vide infra*). The second are excitations with charge transfer character that lie below the optical band gap of Y6 in the thin film phase. To differentiate these states from the higher energy CT states mentioned above, we will refer to these lower energy excitations as ‘polaron pairs’ (PPs). We believe that it is these polaron pair states that are responsible for the debate in the field over whether Y6 can intrinsically generate free charge carriers, a point to which we will return in the experimental results.

With this in mind, we start our analysis by investigating salient features characterizing the absorption spectra of Y6 in dilute solutions of Toluene (TOL) and Chloroform (CF). We report the measured solution spectra in Fig. 1c and give details about the experimental measurements in the Methods. In both solvents, we observe an intense absorption peak corresponding to the transition energy, $E^{(sol)}_{S_0 \rightarrow S_1}$, from the ground ($S_0$) to the first excited state (S_1) and the associated vibronic progressions. $E^{(sol)}_{S_0 \rightarrow S_1}$ is 712.5 nm (1.74 eV) in TOL and 733.6 nm (1.69 eV) in CF (purely electronic, 0–0 transition). The additional band ~0.40 eV higher in energy than $S_0 \rightarrow S_1$ is related to a second electronic transition (*i.e.*, $S_0 \rightarrow S_2$) characteristic of the C_{2v} symmetry point group of the Y6 molecule, as observed in previous work [33,34]. This is confirmed, as shown in the Supplementary Information (SI) Section S3, by employing a Franck-Condon (FC) fitting model expanded to include multiple electronic transitions and vibrational modes for each electronic excitation [33]. Interestingly, in Fig. 1c, we further observe a modest positive solvatochromism upon increasing the polarity of the solvent (*i.e.*, a red-shift going from TOL with a dielectric constant of 2.38 to CF with a larger dielectric constant of 4.81), which is typical of push–pull dyes characterized by a small degree of intramolecular charge separation in the ground state [35]. Associated to such a red-shift we can also see a smearing out of the vibronic spectral features, though the ratio between the intensity of the first vibronic 0–1 band and the main transition, the so-called Huang-Rhys factor ($S_{\mathrm{eff}} = \frac{I_{1-0}}{I_{0-0}}$) [31], is not significantly affected (see Table 1).

TABLE 1

Comparison between measured and computed experimental features of Y6.

<table>
<tr><th>Experiments</th><th>Toluene</th><th>CF</th></tr>
<tr><td>$E^{(\mathrm{sol})}_{\mathrm{S_0 \to S_1}}$ [eV]</td><td>1.74</td><td>1.69</td></tr>
<tr><td>$E^{(\mathrm{thin-film})}_{\mathrm{S_0 \to S_1}}$ [eV]</td><td colspan="2">1.51</td></tr>
<tr><td>Total Red-shift [eV]</td><td>−0.23</td><td>−0.18</td></tr>
<tr><td>S_{eff} solution</td><td>0.37</td><td>0.37</td></tr>
<tr><th>Theory</th><th>Toluene</th><th>CF</th></tr>
<tr><td>$E'^{,(\mathrm{sol})}_{\mathrm{S_0 \to S_1}}$ [eV][a]</td><td>1.82</td><td>1.79</td></tr>
<tr><td>$E^{(\mathrm{sol})}_{\mathrm{S_0 \to S_1}}$ [eV][b]</td><td>1.76</td><td>1.73</td></tr>
<tr><td>Δ_{0-0}[eV][c]</td><td>−0.19</td><td>−0.16</td></tr>
<tr><td>$E^{(\mathrm{cry})}_{\mathrm{FE}}$[eV][d]</td><td colspan="2">1.57</td></tr>
<tr><td>Aggregation Shift [eV][e]</td><td>−0.050</td><td>−0.050</td></tr>
<tr><td>$E^{(\mathrm{cry})}_{\mathrm{S_0 \to S_1}}$ [eV]</td><td colspan="2">1.52</td></tr>
<tr><td>Total Red-shift [eV]</td><td>−0.24</td><td>−0.21</td></tr>
<tr><td>S_{eff} solution</td><td colspan="2">0.33</td></tr>
</table>

[a] Vertical excitation energy in solution.

[b] Adiabatic excitation energy obtained subtracting the relaxation energy ($\lambda^{\mathrm{rel}}_{hf}$ in Table S1) evaluated in the harmonic approximation from the vertical excitation energy as described in the text.

[c] Solution-to-Crystal shift (STCS) evaluated as $\Delta_{0-0} = E^{(\mathrm{cry})}_{\mathrm{FE}} - E^{(\mathrm{sol})}_{\mathrm{S_0 \to S_1}}$ as described in the text and Methods.

[d] Site energy relative to the excitation of a single molecule embedded in the crystal (see Methods and Section S8).

[e] Red-shift due to aggregation effects and mixing between FE and CT states. The minus signs appearing in the energy values indicate a shift toward lower energy.

We now turn to the analysis of the experimental absorption spectrum of Y6 thin-film phase prepared by spin casting the material from solution on the substrate, as described in the Methods. Notably, there is experimental [16,17] and theoretical [14,15] evidence that Y6 film processed from CF solution maintains an extended crystalline structure (see Section S13 and Fig. S11 for an analogue discussion about Y6 film prepared from chlorobenzene). Grazing incident wide-angle X-ray diffraction (GIWAX) measurements show that CF-processed Y6 adopts an ordered face-on orientation on the substrate in its thin-film phase and molecular dynamics simulations reveal crystalline domains with molecules arranged similarly to what is found in the crystal structure. In addition to GIWAXS, there is also experimental evidence from atomic force microscopy (AFM) studies to support the semi-crystalline nature of Y6. AFM imaging performed in Ref. [37] has revealed regions with ordered lattice fringes as larger as 40–110 nm, which are indicative of crystalline domains within the film. Additionally, previous work that has compared the Y6 single crystal to the neat spin-coated film has shown that the intermolecular distances between the core and end groups of Y6 molecules is very similar in both [38]. The similarity between the Y6 packing motif in the thin-film and single crystal was further confirmed by the work of Bi et al. who found that the crystalline domains of Y6 exhibited a structure very similar to the single crystal [39]. For all these reasons, although it would be informative to have experimental data directly on a single crystal for direct comparison with our simulations (see Section S1), we believe that the salient features predicted by the theory on single crystals as discussed below are representative of the ordered Y6 films investigated here.

The CF-processed Y6 thin-film absorption spectrum is reported in Fig. 1c. The transfer matrix modelling (TMM) approach developed by Kerremans et al. [40] has been used here to correct the absorption coefficient for interference and thickness dependence effects (see Methods and Section S12 for details). By comparing the thin-film spectrum with the corresponding Y6 spectrum in CF solution (Fig. 1c), we clearly see three noticeable features: (i) a remarkably large red-shift (~0.18 eV for CF and 0.23 eV for TOL) upon aggregation, (ii) an increase of the 0–1 band by more than a factor of two in the thin-film phase with respect to the solvated single molecule and (iii) a significant broadening of the Y6 aggregate absorption spectrum. The red-shift going from solution to the thin-film phase is a common feature of ideal J-type excitonic interactions where the optically allowed state is at the bottom of the excitonic band of the aggregate [32,84]. The width of the related energy band depends on the strength of the excitonic interactions between the molecules. For ideal J-aggregates, the stronger these interactions, the more red-shifted the spectrum. At first, it may seem plausible to assign the strong red-shift (feature (i)) to strong J-like interactions in Y6 aggregates. However, ideal J-aggregates, or aggreates where J-like character dominates as for instance in m-4TICO (an NFA of the ITIC family) [84], actually show a decrease in the intensity of the vibronic 0–1 side band (relative to 0–0) and a reduction in spectral broadening [32]. Both these characteristics are in contrast with features (ii) and (iii) observed in Y6 aggregates. Additionally, a number of experimental investigations [7,9,11,41] anticipate that potential Y6 CT states might interact with Frenkel-type excitonic states. This could have an impact on the optical properties and the shape of the spectra, as previously observed in other systems [31,42–44]. To understand all these peculiarities of Y6 steady-state optical properties, we turn to state-of-the-art excited-state electronic structure calculations connected to large-scale model Hamiltonians that are necessary to describe extended aggregates.

Y6 steady-state simulated absorption

We have simulated the spectral features of Y6 in solution using high-quality Bethe Salpeter equation (BSE) calculations with the inclusion of a polarizable continuum model (PCM) to simulate the effect of the solvent, as detailed in Methods [24,25]. In Fig. 1d, we achieved a remarkably good agreement (within ~0.1 eV tolerance) with respect to measured absolute excitation energies in both TOL and CF solutions. BSE/PCM provides accurate vertical excitation energies ($E'^{,(\mathrm{sol})}_{\mathrm{S_0 \to S_1}}$) as reported in Table 1 and is able to accurately recover the solvatochromic red-shift observed in the experiment by changing the dielectric constant of the medium. From the vertical excitation energies in both solvents, the corresponding adiabatic energies, to which the main peak ($E^{(\mathrm{sol})}_{\mathrm{S_0 \to S_1}}$) of the simulated spectra is referred, can be estimated by subtracting the relaxation energy of the $\mathrm{S_1}$ state from $E'^{,(\mathrm{sol})}_{\mathrm{S_0 \to S_1}}$. The relaxation energy is evaluated in the harmonic approximation as explained in Section S3 and it is decomposed in terms of frequency-resolved normal modes (see Fig. S3). As done in previous works [31], we assume that such a relaxation is driven by a single effective vibrational mode that couples the excitation to $\mathrm{S_1}$ state (Fig. 1d) and is responsible for the vibronic progression

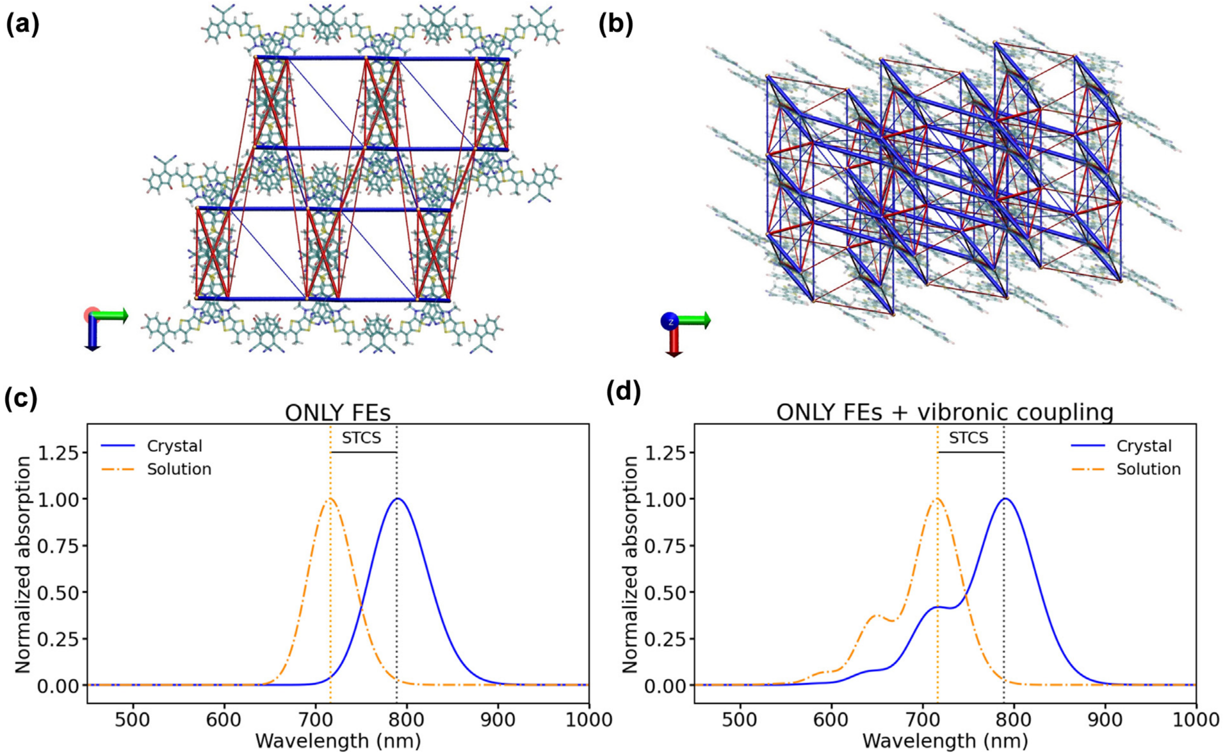

FIG. 2

(a) Top and (b) lateral view of Y6 crystals where H-like (J-like) interactions are shown as blue (red) segments. Only interactions stronger than 15 meV are shown for clarity purpose and the thickness of the coloured lines is proportional to the excitonic coupling strength. In this picture, the H-like (J-like) interactions are defined according to the positive (negative) sign of the transition-dipole-corrected coupling $\widetilde{V}_{kl} = \mathrm{sgn}(\boldsymbol{d}_k \cdot \boldsymbol{d}_l)V_{kl}$, where the term in between parenthesis is the scalar product of the transition dipoles obtained using atomic TrESP charges $\boldsymbol{d} = \sum_I q_I^T \boldsymbol{r}_I$ (*I* runs over the atomic positions of the molecule and q_I^T are the atomic TrESP charges). Panels (c) and (d) show the solution and crystal absorption spectra computed with a pure Frenkel exciton model (H_{FE} in Eq. (2)) with and without vibronic coupling, respectively. The solution to crystal shift (STCS) is indicated in black. Dashed black vertical lines represent the FE energies ($E_{FE}^{(cry)}$) of a molecule in the solid, while the dashed orange ones represent the excitation energies in CF solution ($E_{S_0 \to S_1}^{(sol,CF)}$). Both values are obtained with BSE as explained in the text. No shift is applied to the computed spectra.

observed in Fig. 1c. For this effective mode we computed a frequency, $\hbar\omega_{eff} = 0.18$ eV, characteristic of double C=C bond stretching/aromatic ring breathing (common to other π-conjugated organic systems [31]). The calculated value agrees with resonance Raman experiments that reveal two prominent peaks in the spectrum of Y6 at 0.18 eV and 0.19 eV, respectively (see Fig. S12). This analysis yields an effective Huang-Rhys factor (S_{eff}) associated to $S_0 \rightarrow S_1$ excitation of about 0.33, in line with the experimental observation (see Table 1). By considering the calculated $\hbar\omega_{eff}$ and S_{eff} and using Eq. (S5), we reproduced the vibronic progression of the main $S_0 \rightarrow S_1$ transition in Fig. 1d. We found a good qualitative agreement between the spectral shape of the simulated solution spectra in both solvents with respect to experiments, and we remark that no additional shift has been applied to our simulated spectra. Although in principle we could systematically improve the agreement between the vibronic shape of the simulated solution spectrum, for instance including multiple vibrational modes and electronic transitions (see Fig. S4b) [45], our ultimate goal is to simulate the spectrum of an extended thin-film system. To this end and to keep the model computationally tractable when approaching large systems, considering only a single effective mode per molecular site is a widely used and sensible approximation for this system [31,32].

Compared to the solution case, the description of the optical properties and the electronic excitations in solid state Y6 (Fig. 1b) is complicated by the presence of intermolecular interactions and the larger dimensionality of the system. To accurately describe the spectrum in the crystalline form and explain the spectral features observed in experiments, we used a powerful Frenkel-Holstein Hamiltonian [30–32] (Eq. (1) supplemented by *ab initio* calculations, as described in the Methods section. In brief, such a Hamiltonian is represented on a diabatic basis of localized electronic states of different characters, *e.g.*, single FE states, where electron and hole are on the same site, CT states, where electron and hole sit on different sites (Fig. S5), and it explicitly includes the electronic interactions between them. Namely, the long-range excitonic V_{kl} couplings between tightly bound electron-hole pair sitting either on molecules *k* or *l*, which determine exciton delocalization; photoinduced electron transfer couplings (D_e) and hole transfer couplings (D_h) that allow for exciton splitting into CT states; and electron and hole transfer integrals (t_e and t_h, respectively), which describe the hopping of charges between neighboring molecules, possibly leading to charge separation (see representation in Fig. S5). This Hamiltonian also incorporates the Coulomb attraction between electron and hole as a function of distance, as well as the coupling between electronic and nuclear degrees of freedom. This vibronic coupling interaction is introduced in the model by considering effective modes coupled to the creation of excitonic, cationic and anionic states, as described in Section S3 and Methods.

Holstein-like Hamiltonians as the one used in this work have been employed with great success in previous work [30–32] to describe the optical properties of aggregates and crystals of conjugated organic molecules [32,44,46], supramolecular systems [47], and extended polymers [48,49] and copolymers [50]. However, the novelties of our computational framework over previous work are several, the most important being the following. (i) We move away from ideal lattices of reduced dimensionality with only nearest neighbour interactions [32], in favour of the three-dimensional morphology determined by X-ray diffraction [36]. (ii) The excitation energies that constitute an important part of the Hamiltonian are computed using state-of-the-art BSE calculations coupled to classical polarizable embedding models of atomistic resolution (MM). This formalism allows us not only to retrieve the energy of the FE states, as discussed for the single molecule in solution, but also to accurately determine the energetic position of CT excitations that are notoriously challenging to capture with conventional time-dependent density functional theory (TDDFT) [51]. Furthermore, this approach also permits to accurately account for environmental (electrostatic and dielectric screening) effects [24,25,27–29], which are of great importance for our analysis, for instance, in the remarkable solution-to-crystal shift described below. (iii) We account for the complete range spanned by the long-range excitonic interactions (*i.e.*, beyond nearest neighbour interactions); all being computed from first principles methods that account for the atomistic details of the interacting molecules. The proposed theoretical protocol, detailed in Methods, represents an important step towards a realistic description of the electronic states and optical properties of application-relevant molecular extended systems.

Once constructed, the Hamiltonian is diagonalized to determine the excitonic states needed to generate the absorption spectrum of the Y6 single crystal (Eq. (S4)). The Y6 crystal structure (Fig. 1b) used for the calculations is described in Section S1. The resulting theoretical spectrum is presented in Fig. 1d for a 3 × 3 × 3 supercell in periodic boundary conditions and compared to the experimental counterpart in Fig. 1c. We note that the agreement both in terms of peaks position and relative intensity is excellent. We were able to capture all the key features observed in experiments, including the significant red-shift (calculated to be 0.21 and 0.24 eV) between the CF or TOL solutions and solid-state phase, and the corresponding enhancement of the 0–1 vibronic band. These characteristics are quantitatively reproduced by our simulations (see Table 1). Furthermore, we successfully reproduced the larger broadening of the solid-state spectrum compared to the solution counterpart. Convergence of the results in terms of system sizes, robustness with respect to electronic couplings and other technical aspects are shown in Fig. S9. Moving forward, we will discuss the influence of various components in the Hamiltonian and analyse their contribution to the overall shape of the spectrum to better understand the electronic states of the Y6 thin-film phase.

Aggregation effect in Y6: H-like vs J-like interactions

We start our detailed theoretical analysis focussing on the Frenkel exciton block (H_{FE} in Eq. (2) of the Hamiltonian to investigate whether the red-shift from solution to the aggregate is due to Kasha's aggregation effects and strong J-like excitonic interactions. To this end, we computed the off-diagonal elements, V_{kl}, between pairs of molecules k and l extracted from a supercell of Y6. V_{kl} excitonic interactions are approximated using the long-range Coulomb component between transition densities [52], which scale as r^{-3} (r is the intermolecular distance) [18,52,53]. In this work, we used transition electrostatic potential (TrESP) charges to represent molecular transition densities (Eq. (S6)). Notably, this approach allows to go beyond the commonly used point-dipole approximation which is known to result in large overestimation of the excitonic couplings in closely packed solids of large molecules, like Y6 [18]. Parametrization details of TrESP charges and benchmarks on the accuracy of this approach compared to a robust multi-state fragment excitation energy difference-fragment charge difference diabatization method [52,53] are given in Section S6. The excitonic coupling values for the closest contact nearest neighbour pairs are reported in Table S2; they are all sizable, pointing to a strong excitonic effect in Y6. Besides the nearest neighbour, our fast TrESP approach allows us to compute the full range of excitonic interactions in large Y6 crystals quickly and accurately. The use of atomic TrESP charges is also useful to ensure a consistent relative sign of the interaction within the Hamiltonian in Eq. (2). We discuss this important point in more details in Section S6. In Fig. 2a, b, we visually show the amount and strength of J-like interactions in blue vs H-like interactions in red on a supercell. Notably, both H-like as well as J-like interactions are similarly abundant and have similar magnitude in the crystal (*vide infra*). This hints to the fact that the red-shift observed in Fig. 1c might not be a consequence of J-aggregation and we prove this hypothesis below by constructing the full H_{FE} Hamiltonian.

The excitonic eigenstates of H_{FE} were used to calculate the optical aborption spectrum of the crystal due solely to Frenkel exciton according to Eq. (S4). The excitonic couplings refer to the crystal structure using periodic boundary conditions with a minimum image convention to deal with extended systems. These interactions were screened by an isotropic dielectric constant (ε = 2.9), which we computed with the same MM model employed in embedded *ab initio* calculations [29]. This value is consistent with what was measured by Li et al. in Ref. [54] (ε = 3.36). A detailed description of these calculations is provided in Methods. Besides excitonic couplings, we also accurately computed the solution-to-crystal shift (STCS), $\Delta_{0-0} = E_{\mathrm{FE}}^{(\mathrm{cry})} - E_{\mathrm{S}_0\to\mathrm{S}_1}^{(\mathrm{sol,CF})} = -0.16$ eV when going from CF solution to the crystalline phase. Both the solution and the crystal excitation energies has been obtained with embedded BSE calculations, the former adopting a PCM embedding mimicking CF, the second describing the crystalline environment with an atomistic polarizable MM embedding constituting the crystalline environment. The significant STCS mostly arises from the higher dielectric constant of the solid, with respect to the CF solution, plus smaller contributions from electrostatic crystal fields and molecular geometries (see Table S6). Computed energy values are reported in Table 1 and the protocol used for these high-quality calculations is described in Methods.

The FE spectra of the Y6 aggregate without and with vibronic coupling are reported in Fig. 2c and 2d, respectively, and compared to the solution spectrum in CF. We can observe that in both cases the Y6 crystal is red-shifted compared to solution by an amount that essentially corresponds to the STCS (Δ_{0-0}). To support the fact that H- vs J-like aggregation compensate each other and have a null effect on the spectra we calculated the amount and total strength of positive and negative interactions on the converged 3x3x3 supercell used also for the absorption spectra. We found that 48 % of the interactions are positive (defined as H-like), while 51 % is negative (defined as J-like). By summing all the positive interactions and the negative interactions respectively among each other, we found that H-like interactions, although slightly less in number, are overall a factor of 1.1 larger than J-like interactions. The similar amount and strength of J-like vs H-like interactions, along with the relative patters produced by the couplings between sites [55,56], makes it such that the effect of aggregation in Y6 is almost null with only a tiny (3 meV) shift towards the red edge of the spectrum compared to the vertical black dashed line in Fig. 2c (representing $E_{FE}^{(cry)}$).

Fig. 2d shows that considering the vibronic coupling to FE states results in a slight improvement of the overall spectral shape. The coupling to an effective vibration yields the formation of the 0–1 side band observed in experiments. However, the intensity of this vibronic replica is much lower than the 0–0 band, while comparable intensities have been measured in the experimental absorption spectrum of Y6 films (Fig. 1c). Moreover, although the STCS is substantial, the total red-shift going from the solution phase to the aggregate is lower than what we measured. These observations suggest that other contributions, in addition to aggregation and coupling to vibrations of bright FE are still missing from this preliminary analysis.

Intermolecular CT excitations: Impact on the optical properties of Y6

The nature of the primary electronic excitations in thin-films might change considerably upon switching on the interactions between FE and CT states and this should have an impact on the spectral shape. Recent works showed that this might be the case in pristine Y6 [7,10], though the lack of vibronic effects, and the use of routine TD-DFT calculations, whose results are notably functional dependent when it comes to CT state energies, prevented from reaching reliable conclusions. We thus completed the Hamiltonian in Eq. (1) calculating H_{CT} and H_{FE-CT} (Eqs. (3) and (4) matrix elements to account for the formation and mixing between CT and FE states. To this end, we evaluated photoinduced electron and hole couplings and hole and electron transfer integrals (D_e, D_h, t_e and t_h, respectively) between the molecules in the crystal (see Fig. S5) and used accurate diabatization approaches as described in Sections S6 and S7.

Because all these interactions decrease exponentially in magnitude with increasing distance, as they essentially depend on the orbital overlap of the interacting molecules, we computed them in Y6 for all the pairs within a maximum distance cut-off of 20 Å from each other. Among all these unique pairs, eight of them (D1 to D8 in Fig. S2) have a minimum distance between atoms below 5 Å and are in nearest-neighbor contact. Among these eight pairs, six pairs with a minimum interatomic distance below 3.5 Å exhibit non-negligible (*i.e.*, above 0.1 meV) electronic couplings (see Table S3), whereas the other two have negligible FE-CT coupling. It is worth noticing that these interactions are in some cases larger in magnitude than related excitonic couplings, pointing to strong possible mixing between FE and CT states. Nonetheless, it is also crucial to quantify the energy of the CT states to establish to which extent the energy level alignment compared to the couplings between FE and CT states is sufficiently favourable to modify the spectral shape and photophysics of the crystal [43]. To this end, we quantified the energy of CT-like excitations as a function of electron-hole distance, $E_{CT}(r_s)$, using BSE calculations with polarizable MM embedding performed on some of the representative pairs extracted from the crystal. From these data, we derived a (screened) Coulomb barrier (see Fig. S8), describing the energetics of electron and hole particles at various distances and completed the Hamiltonian in Eq (1). Details on such calculations and parametrization of the energy barrier are given in Section S9. We found that the diabatic, pure, nearest-neighbour CT pairs are about ~0.1 eV above the energy of localized FE states, which confirms that FE and CT states can potentially strongly mix and modify the optical properties of the aggregate. We note that, a similar conclusion has been recently and independently reached in Ref. [57].

Our data allows us to estimate an exciton binding energy, E_b, in Y6 crystal and compare it to experiments. The experimental measurements of E_b reported is reported by Karuthedath et al. [58] obtained by combining photoemission (direct and inverse photoelectron spectroscopy) and optical (absorption and emission) data. The reported difference between the optical and the photoemission gap is $E_b \sim 0.25$ eV. We estimated a higher exciton binding energy, E_b, in Y6 crystal of ~0.5 eV, computed as the difference between the energy of separated charges at infinite distance and the closest bound diabatic CT state in Fig. S8 (see Section S10). This value is not inconsistent with the experiment as it does not include the effect of narrowing in the solid state due to intermolecular charge delocalization and energetic disorder [29,59]. These two effects typically reduce the transport gap by a few hundreds of meV, making our estimates consistent with experimental data. The relatively large E_b suggests against the facile generation of free charges starting from bound electron-hole CT pairs in pristine Y6 crystal. This point will be further investigated in the experimental section.

The spectra obtained from the diagonalization of the full Hamiltonian in Eq. (1) are shown in Fig. 3, without and with the inclusion of local vibronic coupling introduced using Eqs. (5)–(7) (see panel a and b, respectively). Interestingly, in both cases we note a shift of the main 0–0 peak of the aggregate towards lower energy compared to E_{FE} (dashed black line). This additional red shift (of ~50 meV) acting on top of the STCS is a direct consequence of the interaction between FE and CT states. Specifically, the mixing between these states gives rise to hybrid FE-CT states which are pushed down in energy similarly to what

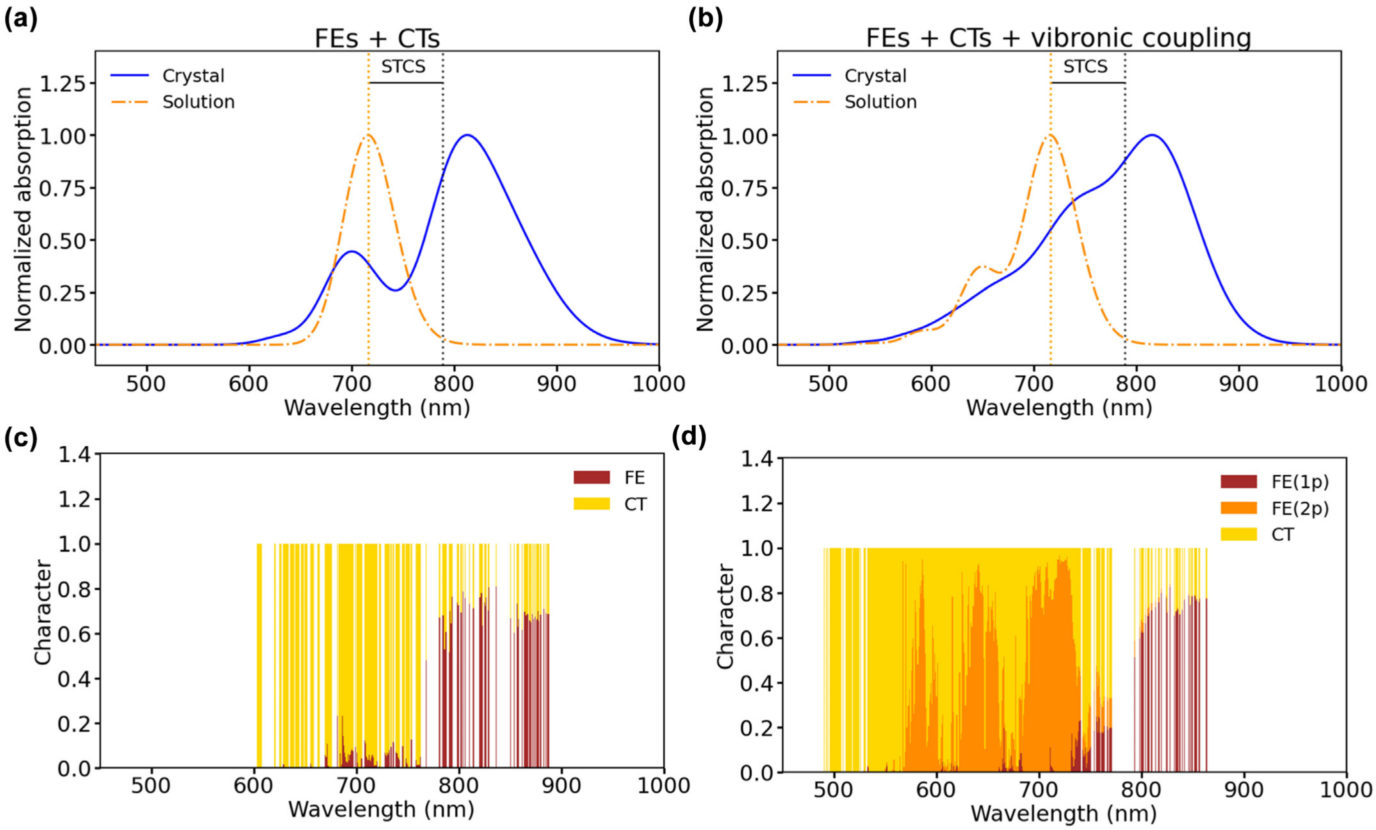

FIG. 3

Panels (a) and (b) represent the computed and solution aggregate spectra without and with local vibronic coupling, respectively, obtained using the full Hamiltonian in Eq. (1). Panel (b) shows the same data as Fig. 1d. The STCS is indicated. Dashed black vertical lines represent the FE energy ($E_{\mathrm{FE}}^{(\mathrm{cry})}$), while the dashed orange ones represent the excitation energy in CF solution ($E_{S_0\to S_1}^{(\mathrm{sol,CF})}$). Both values are obtained with BSE/MM as explained in the text. No shift is applied to the computed spectra. Panel (c) and (d) depict the character of the eigenstates of the Hamiltonian as a function of their energy and the related FE-CT mixing without and with the inclusion of vibronic coupling in the Hamiltonian, respectively. When the vibronic coupling is included FE one-particle and two-particles states (indicated with 1p and 2p) are depicted with different shades of orange (see Methods for details).

was found by Spano et al. for perylene-based dyads, donor-acceptor-donor chromophores and other 1D systems [30,42,43]. In these cases, the interference between short-range photoinduced hole/electron transfer couplings and Coulomb interaction gives rise to "red-shifted HJ aggregates" depending on the phase of the interactions. In Fig. 3c, d, we report the character of the adiabatic states of Y6 crystal as a function of their energy (calculated with Eqs. (S11)–(S13)) and we clearly show that FE and CT states can mix to a different degree depending on the position in adiabatic energy space. Taking into account the associated red-shift now results in excellent agreement with the experiment absorption spectrum reported in Fig. 1c.

As shown in Fig. 3b, including the coupling to vibrations generates a vibronic shoulder in the spectrum, analogous to that in Fig. 2d where only FE states were considered. However, the relative intensities of the 0–0 and 0–1 vibronic replica dramatically change between the pure FE and the hybrid FE-CT model, the latter showing a much more prominent 0–1 band, in excellent agreement with the normalized experimental absorption on film (see Fig. 1c). By comparing the absolute intensity of the spectra without and with CT states, we can observe that the intensity of the 0–1 band remains roughly constant, but the intensity of the main 0–0 transition decreases when CT states are included (see Fig. S10). This is because the bright FE states at the onset of the absorption becomes strongly mixed with CT states (Fig. 3c, d) and lose part of their oscillator strength (compared to the pure FE case). Overall, this has the effect of reducing the ratio between the 0–0 and the 0–1 intensities when CT states are included in the Hamiltonian.

Finally, moving the attention to the blue edge of the spectrum (*i.e.*, ~690 nm) in Fig. 3c, d, we observe that the initially dark CT states become slightly dipole allowed by modestly borrowing oscillator strength from vibronic FE states. This mixing is driven by the large density of pure CT states available at these energies and significantly broadens the aggregate spectrum with respect to the one in solution, thereby explaining also such an evident feature of the measured spectra shown in Fig. 1c. On the contrary, when only FE states are considered (Fig. 2d), the spectral broadening does not change going from solution to the aggregate.

We conclude this section by noting that our theoretical investigation suggests the red-shift in Y6 is not a result of H- versus J-aggregation, as occurs in other NFAs [84], but rather arises from polarization effects and the interaction between FE and CT states, as discussed earlier. Our calculations reveal that interactions between FE and CT are crucial to promote hybridization

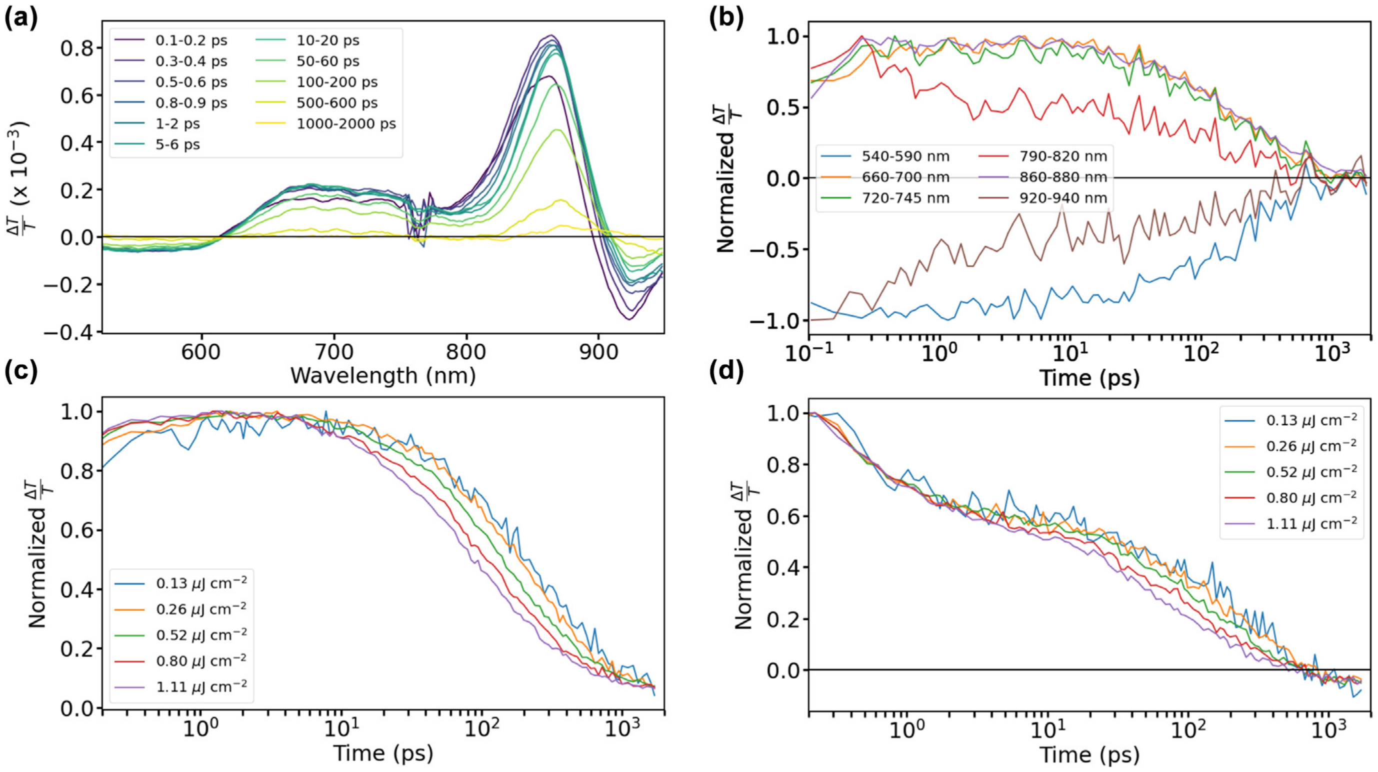

FIG. 4

(a) Y6 neat (100 wt%) film visible probe ps-TAS spectra. Note that the noise around ~765 nm is due to pump scatter in this region. (b) Kinetics normalized to maximum, fluence = 0.61 μJ cm^{-2} (λ_{pump} = 765 nm). Panels (c) and (d) depict Y6 neat film NIR probe ps-TAS fluence series for (c) 860–870 nm kinetic and (d) 920–960 nm kinetic (λ_{pump} = 800 nm). In the latter two panels, kinetics are normalized to the maximum for each fluence.

of states of different character. Besides high electronic couplings, another crucial factor is the energetic proximity of CT and FE states.

Time resolved spectroscopy of Y6 thin-films

To gain a deeper understanding of the excited-state dynamics in thin-film phase Y6 and how they fit in with our computational results, we turn to TAS. In Fig. 4a, we show the TAS spectrum of a neat Y6 film with excitation at 765 nm. Like the solution TAS measurement (reported in Fig. S13), the thin-film possesses a central ground state bleaching (GSB) in the region of 615–900 nm, flanked by two photo-induced absorption (PIA) bands; one centred at 550 nm and the other at 930 nm. However, it is informative to consider the form of the TAS spectrum in more depth. Specifically, the GSB exhibits a noticeable dip in the centre, approximately ranging from 700 to 825 nm, that does not match the reported steady-state absorption spectrum (Fig. 1c). As expanded on below, we therefore propose that this discrepancy in the spectral shape is caused by the presence of additional PIA underneath the GSB band.

Through comparison to TAS measurements on BHJ blends of Y6 with three commonly used electron donating polymers (Fig. S16), we assign this PIA band underlying the GSB to the (electron) polaron of Y6 (see Section S14 for discussion of the assignment). However, the PIA band centred at ~780 nm in the BHJ blends is more pronounced than in the neat Y6 film, to the extent that it dominates over the Y6 GSB feature located above it. Hence, in-line with previous reports [11,12,7,9], there is an initial indication that polaronic-like states may also be present in the neat film of Y6, albeit formed with a lower yield than in the BHJ blends. To provide further evidence for the formation of polaronic states in Y6, Fig. 4b shows the normalized TAS kinetics taken from different spectral regions of the neat Y6 film. Most of the kinetics exhibit a single decay component. However, two kinetics in the 790–820 nm and 920–940 nm range are biphasic and display an additional fluence-independent sub-picosecond component. The PIA around 930 nm has previously been assigned to the singlet exciton state in Y6 [9]. However, our calculations suggest that the initially photogenerated state will be specifically a FE-CT hybrid excitation, rather than a pure singlet exciton, though the FE-CT excitation performs essentially the same function in Y6. Nonetheless, the decay of this state, which matches the growth of the Y6 polaronic PIA underneath the GSB, further confirms the conversion of FE-CT hybrid states into polarons in neat Y6. Our ability to fully resolve this FE-CT hybrid excitation to polaron conversion process is limited by the instrument response of ~200 fs for this TAS dataset. Thus, we have also performed additional TAS measurements with an ultrafast (<20 fs) excitation pulse (Fig. S19). Exploiting the superior time resolution, a kinetic taken from the FE-CT hybrid state PIA between 920–940 nm reveals that its intensity reduces by ~60 % by 2 ps after excitation, before plateauing (Fig. S20). This allows us to estimate that 60 % of photogenerated excitations in a neat Y6 film form polaronic states, whilst 40 % occupy the FE-CT hybrid state manifold.

In-line with the observations of Wang et al., we find an additional PIA at 1550 nm in the neat Y6 film that is formed on the same timescales that the 930 nm FE-CT hybrid state PIA is quenched on (see Fig. S17) [9]. This implies that the origin of this 1550 nm PIA may also be polaronic. Curiously, when examining the dynamics of the BHJ blends, we find that the 1550 nm PIA is quenched by hole transfer from Y6 to the polymer (Fig S15). To further probe the origin of this absorption signature, we have performed spectroelectrochemical measurements on a neat Y6 film (Fig. S24). See details of the measurements in Methods. Under oxidation, we observe the formation of a new polaronic absorption band at 0.89 eV (1380 nm), close in energy to the 0.80 eV (1550 nm) PIA band in the TAS of neat Y6. We note that the different counterion (PF_6^- in the spectroelectrochemistry vs $Y6^-$ in the TAS) could impact the hole polaron localisation and thus account for the small (<0.1 eV) energy difference of the measured transitions [60]. Therefore, as the 1550 nm PIA band shows a close match to the new infrared absorption feature in an oxidised Y6 film and is also quenched by hole transfer in the BHJ blends, we assign this feature to the hole polaron of Y6.

As an additional tool to probe the exciton to polaron conversion process, we have dispersed the Y6 molecules at 50 wt% in the non-interacting wide bandgap host material 3,3′-Di(9H-carbazol-9-yl)-1,1′-biphenyl (mCBP). TAS measurements reveal that diluting Y6 in the solid-state results in a slowing of the polaron formation (Fig. S15). Consequently, the spectral shape of the GSB at 0.1–0.2 ps much more closely resembles the steady-state absorption of neat Y6, before the polaronic PIA at 780 nm grows in over slightly longer (picosecond) timescales. By 10–20 ps, the spectral form in the mCBP dispersion has evolved to match that of neat Y6, indicating the process converting FE-CT hybrid states into polarons is completed by this time. Therefore, it is apparent that the formation of the polaronic states in Y6 is extremely sensitive to the dispersion of the Y6 molecules and the resulting disruption in the formation of extended Y6 aggregates.

In Fig. S18, each kinetic taken from the TAS of Y6 is normalized to its value at 2.5 ps, and it can be observed that all the kinetics exhibit similar decay thereafter with a time constant of ~300 ps. Consequently, recovery to the ground state of most electronic excitations present after 2.5 ps is governed by the same process. The fluence dependence of the recombination kinetics is illustrated in Fig. 4c and d. Here, we only reach a regime where the excited state decay is fluence-independent at the very low fluences of 0.13 and 0.26 μJ cm^{-2}. This indicates that the recombination of electronic excitations in neat Y6 becomes bimolecular at relatively low excitation densities, consistent with the long excited state diffusion length reported for Y6 [61]. Furthermore, we observe that the 860–870 nm kinetic taken from the peak of the GSB region reaches a plateau at 2 ns with approximately 8 % of its normalized intensity remaining, independent of the fluence. At this point, we find no evidence for a significant remaining population of FE-CT hybrid or polaronic states on Y6, due to the absence of their PIAs at 930 nm, 780 nm, and 1550 nm (Figs. 4 and S21a). The only remaining PIA is that of the Y6 triplet exciton, found at ~1450 nm (Fig. S21c), which has previously been reported to decay via a mixture of monomolecular triplet decay and triplet–triplet annihilation, depending on the triplet exciton density in the film [62]. As the triplet exciton yield is fluence independent, they cannot be formed from the states in neat Y6 that show a strong fluence dependence to their recombination rate, as this would be expected to reduce the triplet yield at higher excitation fluences. Thus, to account for this observation of a fluence-independent triplet exciton yield of ~8 %, we propose the existence of a small but constant proportion of photogenerated FE-CT hybrid states that do not interconvert with the polaronic states, nor show significant bimolecular annihilation at the (low) excitation fluences measured here (see Fig. 4). We attribute this to the creation of FE-CT hybrid states on Y6 molecules located too far from a site where conversion to polarons can occur (vide infra). These FE-CT hybrid states may subsequently undergo intersystem crossing (ISC) to generate the long-lived triplet excitons and are responsible for the observed residual and fluence-independent GSB signal at 2 ns. We believe that this small fraction of relatively long-lived FE-CT hybrid states may also be responsible for the nanosecond photoluminescence decay observed in neat Y6 films [22,23], which exceeds the ~300 ps primary excited state lifetime observed in the TAS.

Our theoretical reproduction of the absorption spectrum for Y6 crystal suggests the presence of a continuum of hybridised FE and CT states, which is responsible for the significant broadening, and some of the red-shift, of the absorption spectrum when moving from solution to the thin-film environment. To test this hypothesis, we have investigated the pump wavelength dependence of the Y6 film TAS. We have selected four further pump wavelengths to excite different energetic regions in the Y6 absorption spectrum: 500 nm (2.48 eV), 650 nm (1.91 eV), 870 nm (1.43 eV), and 950 nm (1.31 eV), as shown in Fig. 5. Excitation at 500 and 650 nm is expected to pump higher lying FE-CT hybrid states, whilst 870 nm excitation will excite the lowest FE-CT transition. By contrast, sub band gap excitation at 950 nm is expected to pump the tail states present in Y6. We find that when pumping the higher lying FE-CT transitions at 500 and 650 nm, there is significant sub-picosecond spectral evolution. This is comparable to the TAS data shown in Fig. 4 with 765 nm (1.62 eV) excitation, where the evolution is particularly prominent in the regions associated with the Y6 polaron (~780 nm) and FE-CT hybrid state (~930 nm) PIAs, but even more pronounced. Curiously, the rapid spectral evolution is reduced, but still present, with 870 nm excitation. The spectral shape only becomes largely invariant at all measured time points when exciting in the absorption tail at 950 nm. This difference is further highlighted in Fig. S22, where the excitation energy-dependent spectra in the early (0.3–0.4 ps) and late (10–20 ps) time regimes are compared. In the early time regime, higher pump photon energies result in an enhanced intensity on the blue edge of the primary GSB peak around 800 nm and a more intense 930 nm PIA. In other words, the TAS spectrum shows the presence of more FE-CT hybrid states with a PIA at 930 nm and fewer polaronic states with a PIA at 780 nm. However, by 10–20 ps, the spectra become identical, indicating that the composition of the system is the same at this time regardless of the initial excitation wavelength. The amount of ultrafast evolution,

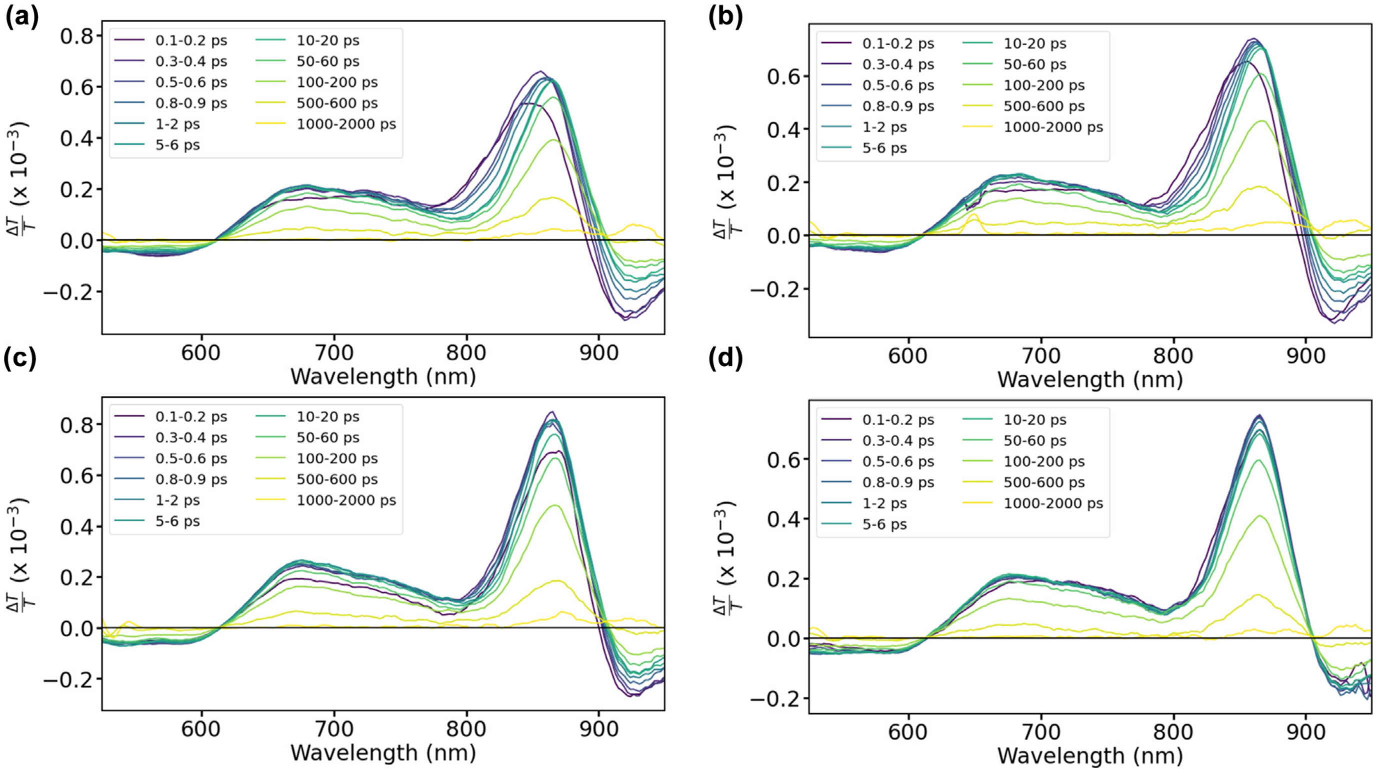

FIG. 5

Excitation-dependent Y6 100 wt% thin-film visible probe ps-TAS spectra at (a) fluence = 2.26 μJ cm^{-2} (λ_{pump} = 500 nm), (b) fluence = 1.38 μJ cm^{-2} (λ_{pump} = 650 nm), (c) fluence = 0.98 μJ cm^{-2} (λ_{pump} = 870 nm), (d) fluence = 19.5 μJ cm^{-2} (λ_{pump} = 950 nm).

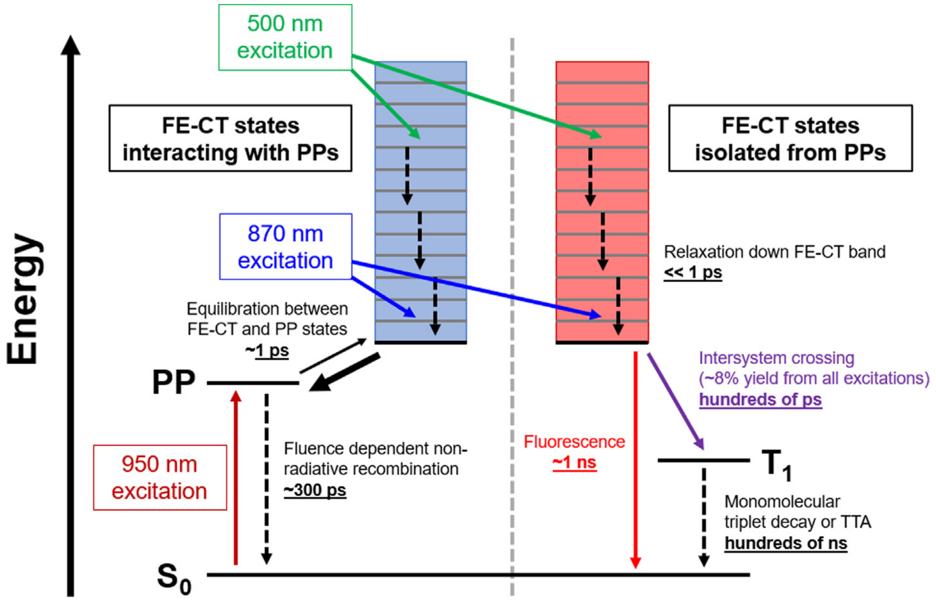

FIG. 6

A schematic representation of the excited state dynamics of Y6 thin-film. To explain the complex Y6 photophysics, we propose presence of two distinct Frenkel exciton-charge transfer (FE-CT) hybrid excitation manifolds in the neat Y6 film: one that can interact with the polaron pair (PP) states observed experimentally, and one that cannot. The timescales of the relevant electronic processes occurring in Y6 are also given in the diagram.

which increases as the excitation photon energy rises, supports the calculation results of a dense continuum of hybridised FE and CT states through which the electronic excitation relaxes on sub-picosecond timescales, before eventually forming the final state with more polaronic character (see Fig. 6). However, the continued presence of some spectral evolution with 870 nm excitation, which disappears with 950 nm excitation, suggests that the state with polaronic PIA signatures is not the state formed directly when exciting the lowest FE-CT transition of Y6. This points to the presence of additional, lower energy, polaronic states in Y6 films, distinct to the FE-CT manifold, that can only be directly accessed by sub band gap excitation at 950 nm.

Finally, it is necessary to address the unusual behaviour of the FE-CT hybrid state PIA at 930 nm in the neat Y6 film. Specifically, two observations: (i) why the FE-CT hybrid states are not fully converted into the lower energy polaronic states, as seen by the PIA band at 930 nm retaining ~40 % of its initial intensity beyond the timescales (>2 ps) of the polaronic state formation (Fig. S20); and (ii) why the PIA signature of the FE-CT hybrid states is present when directly exciting the polaronic states below the band gap at 950 nm. To explain these observations, we compare the kinetics taken from the FE-CT hybrid state PIA at 925–935 nm for the pump wavelength series in Fig. 5. For 500, 650, 765, and 870 nm excitation, there is a clear partial sub-picosecond quenching of the FE-CT hybrid state PIA as it is converted into the polaronic state. However, with 950 nm excitation, we note that the FE-CT hybrid state PIA instead shows a slight growth within the first picosecond after excitation, the rise of which we are likely unable to fully resolve due to the ~200 fs instrument response of this TAS measurement. As lowering the photon energy by 130 meV is enough to move from exciting the lowest FE-CT hybrid states to the sub band gap polaronic states, they are both clearly located close in energy. Thus, we conclude that the FE-CT hybrid and polaronic states in Y6 are in a dynamic equilibrium, which is why their PIA signatures co-exist and there is evidence for their interconversion in the TAS. A dynamic equilibrium between FE-CT hybrid and polaronic states can also explain the largely identical decay kinetics seen across all spectral regions after 2.5 ps in Fig. S23, as both manifolds can share a common dominant (non-radiative) recombination pathway, likely via the polaronic state manifold.

For convenience, we have summarised the proposed states and their photophysics following optical excitation in Fig. 6. This revolves around the presence of two distinct FE-CT hybrid state manifolds, one of which can interact with the polaron pair (PP; vide infra) states, whilst the other cannot. The former manifold of ‘interacting’ FE-CT states is responsible for the polaron pair formation and the majority of the (non-radiative) recombination, whilst the latter ‘isolated’ FE-CT states mediate the nanosecond fluorescence and fluence-invariant triplet exciton yield via ISC also observed in neat Y6 films.

The nature of the polaronic states in Y6 films

Our experimental results thus far indicate that most photogenerated electronic excitations in Y6 eventually form states with polaronic signatures, independent of the excitation photon energy. However, we note that such a low-lying polaronic state is not captured by our computational models based on the crystal structure data of Y6. Thus, when combined with our experimental evidence pointing to the presence of a sub band gap polaronic state, we conclude that polaron formation is not an intrinsic property of the FE-CT hybrid excitations of Y6 aggregates, but rather results from regions of the ‘real world’ Y6 film that are not present in the ‘perfect’ single crystal environment. This could include defect sites in the molecular packing motif or boundaries between crystalline domains in the Y6 film. For example, in a recent report on single-component α-sexithiophene device that gave a power conversion efficiency of 2.9 %, a plausible explanation for free polaron generation was proposed based on electrostatics at the interface between crystalline domains possessing distinct orientations [20]. It is possible that a similar electrostatic effects could also be present in neat Y6 films, as indicated in a recent publication by Fu et al. [17].

As there is currently significant debate on this topic [7,11,22], it is important to clarify whether these polarons have a significant separation and can be considered free charge carriers (defined as when the electron and hole separation exceeds their Coulomb capture radius of ~5 nm [21] or whether they represent more tightly bound polaron pair states, potentially located on neighbouring Y6 molecules. On this point, we first note that the lifetime of the polaronic states in the TAS of neat Y6 films is on the order of ~300 ps in the fluence-independent regime. Given the short, sub-nanosecond lifetime, we consider that this already provides good evidence that the polarons do not achieve long range charge separation; the free charge carrier lifetimes reported in organic solar cell blends of PM6:Y6 are on the order of tens of microseconds in TAS measurements with comparable, or slightly higher, excitation fluences [12]. Thus, it seems implausible that neat Y6 should also generate polarons that achieve a separation exceeding the Coulomb capture radius of ~5 nm [21], yet decay four to five orders of magnitude more quickly than in the PM6:Y6 BHJ. Even when considering that the BHJ morphology can assist with keeping the electrons and holes separate.

To better understand the nature of the polaronic states in neat Y6 films, we turn to magnetic resonance techniques (see Methods). Magnetic resonance spectroscopies are uniquely sensitive to the presence of unpaired spins in a sample and are thus well placed to probe electronic excitations with a non-zero spin, such as polarons, (triplet) charge transfer states, and molecular triplet excitons. We begin by exploring Y6 with transient electron paramagnetic resonance (trEPR) spectroscopy. Fig. 7a shows the trEPR spectrum of neat Y6 film. The full-field (FF) spectrum (280–420 mT) corresponds to $\Delta m_S = \pm 1$ transitions between triplet sublevels, whilst the width of the FF signal is a measure of the Zero-Field Splitting (ZFS) parameter D, which in organic semiconductors is determined by the dipolar interaction and thus correlated to the inter-spin distance r ($D \propto r^{-3}$) [63]. The D value is given by D = 940 MHz characteristic for Y6 molecular triplet excitons [64,65], whilst the *eeeaaa* polarization pattern (*e* = emission, *a* = absorption) is typical for triplet excitons formed via ISC with a zero-field population of p_z, p_y, p_x = 0, 0.66, 0.34. However, it is

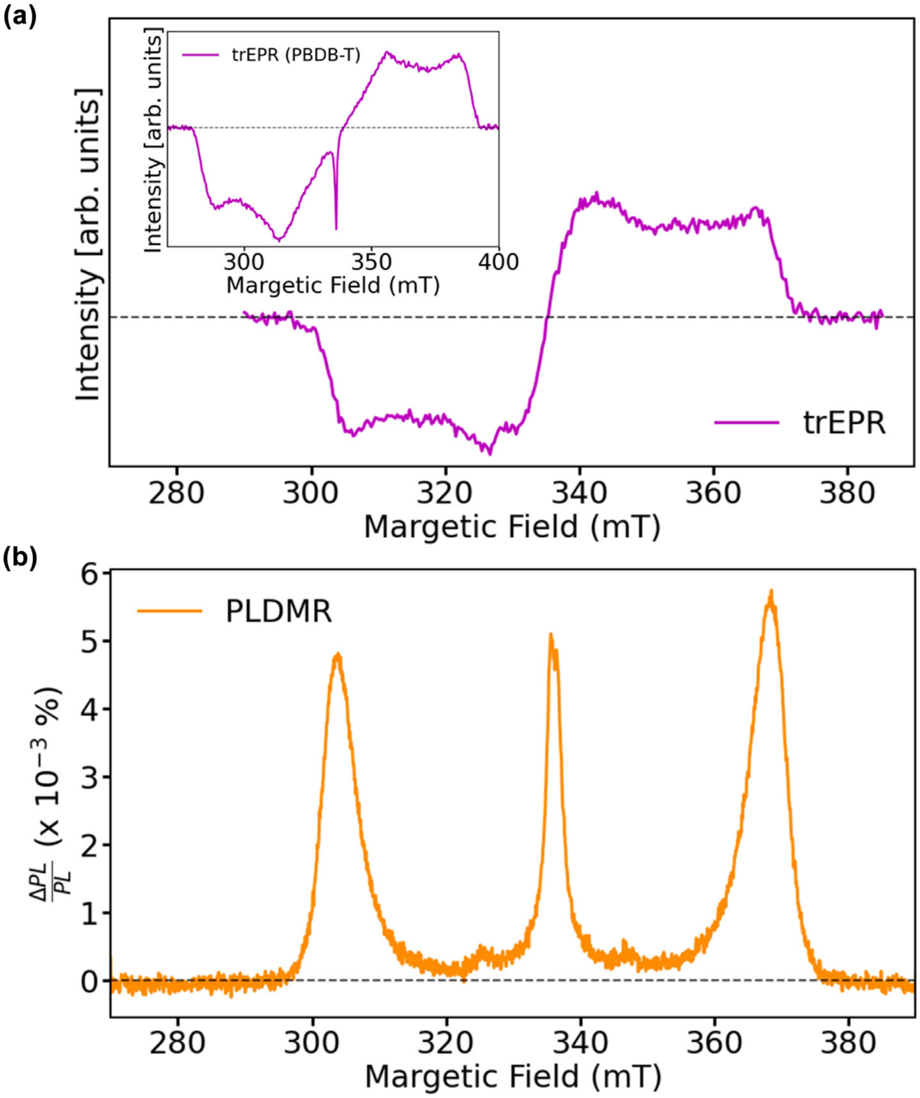

FIG. 7

Magnetic resonance measurements on neat Y6 films. (a) trEPR spectrum for a neat Y6 film (inset: trEPR spectrum for a neat PBDB-T film). λ_{pump} = 532 nm. (b) PLDMR spectrum of a neat Y6 film λ_{pump} = 473 nm. All measurements were performed at T = 10 K.

pertinent to compare Y6 to other organic semiconductor materials that are known to form a small quantity of free polarons in neat films, such as conjugated polymers [66]. One example is the commonly used OPV electron donor polymer PBDB-T [67], for which the trEPR spectrum is shown in the inset of Fig. 7a. As well as the broad molecular triplet exciton feature, we also observe the presence of a narrow feature at ~336 mT. The small width of this feature and the presence of a single peak, as opposed to a more complex polarisation pattern with several emissive and absorptive peaks typical of a charge transfer state [68], indicates that it originates from free polarons. By contrast, this signature is absent in Y6. Whilst it is worth noting that the time resolution of trEPR is on the order of hundreds of nanoseconds and the TAS measurements suggests the majority of excited state recombination in Y6 occurs sub-nanosecond, the absence of a polaron signal further suggests that the formation of long-lived free polarons in Y6 is a negligible pathway following photoexcitation. An even more sensitive magnetic resonance method with optical detection and cw-light excitation is photoluminescence-detected magnetic resonance (PLDMR). Fig. 7b shows the PLDMR spectrum of a spin-coated Y6 film. The same Y6 molecular triplet exciton observed in the trEPR is also seen here in the pronounced spectral 'wings' at ~303 and 386 mT. The details of the molecular triplet exciton in the PLDMR spectrum of Y6, including its link to the strong molecular ordering face on to the substrate of Y6, has been discussed previously [65]. However, we also note the presence of a narrower feature around$g$ = 2. The linewidth of this feature in neat Y6 is 2.5 mT (see EasySpin simulations, Fig. S25 and Table S9), which is comparable to reports of charge transfer states located at the donor:acceptor interface in OPV blends, such as PM6:Y6 or PBDB-T:Y6 [65]. By contrast, the PLDMR of neat polymers that showed free polaron features in trEPR, such as PBDB-T, have a smaller linewidth of 1.0 – 1.4 mT (as $D \propto r^{-3}$, a small change in linewidth correlates to a significant difference in the interspin distance, r) [65]. Note that for weakly-interacting spins, the two transitions probed in PLDMR between the $m_s = 0$and $m_s \pm 1$ sublevels of the (triplet) charge transfer state (equivalent to the polaron pair state discussed here for Y6), will merge and appear as a single inhomogeneously broadened Gaussian curve [65]. Thus, when considered together with the absorption signatures of polaronic states in the TAS and the absence of free polarons in the trEPR, the PLDMR results suggest that the polaronic states present in neat Y6 may be polaron pairs with a small intermolecular separation. However, further PLDMR studies are required to identify the precise nature of the polaronic states in Y6 and their paramagnetic properties, which are beyond the scope of this work. Based on the present evidence, whilst it is plausible that these polaron pair states may possess a reduced binding energy that renders them more susceptible to separation in a single-component Y6 OPV device, potentially at the interface with the hole and/or electron transport layers or assisted by an electric field applied across the device, we conclude that free polarons are likely not the primary photoexcitation in neat Y6 films.

Conclusions

We have shown that high-quality electronic structure calculations combined with a reliable description of the environmental response, both in solution and in the solid state, account for the experimentally observed spectral changes upon crystallization in the archetypic NFA Y6. Notably, this degree of accuracy is only possible when the energetics of the CT excitations and their mixing with other states is considered. We demonstrated in this way that two major effects are responsible for the observed red-shift going from Y6 solution to its thin-film-phase: (i) strong mixing between closely spaced diabatic FE and intermolecular CT states (with an energy off-set for the closest contact pair being ~0.1 eV in Y6); (ii) a sizable solution-to-crystal shift going from chloroform solution to solid-state Y6, which we calculate to be about 0.16 eV. We have shown that the steady-state optical features of Y6 upon aggregation are strongly influenced by the strength of the intermolecular interactions, for instance the shape and relative intensity of the vibronic shoulder compared to the main absorption band as well as the broadening of the Y6 thin-film spectrum compared to the solution counterpart are directly a consequence of the formation of hybrid FE-CT states.

We have provided experimental evidence for the proposed hybridisation of FE and CT states in Y6 by probing the pump wavelength dependence of the excited state dynamics using TAS. At higher photon energies, there is an increase in the sub-picosecond relaxation effects in the Y6 film, which we attribute to the relaxation of the electronic excitations down the dense manifold of FE-CT hybrid states predicted computationally. However, TAS also reveals the existence of a polaronic state below the lowest FE-CT state, which can be directly accessed by excitation below the band gap of Y6 at 950 nm. We further find evidence that the FE-CT hybrid and polaronic states are in a dynamic equilibrium, as exciting the polaronic states at 950 nm leads to the delayed formation of FE-CT hybrid state signatures in the TAS. However, the short (~300 ps) lifetime of these polaronic states, combined with the absence of any features expected for free polarons in magnetic resonance spectroscopy measurements, suggests that most of these states are bound polaron-pairs, likely located on neighbouring Y6 molecules. The absence of such a polaron pair state in our high-quality electronic structure calculations further implies that the presence of polaronic states is related to factors not captured by the ‘perfect’ single crystal environment, such as defect sites or interfaces between crystalline domains.

Considerations made in this work, which led us to unravel important electronic and spectroscopic features of Y6, likely apply more broadly to other NFAs within the Y-family. For instance, due to the specific and complex crystal packing, the effects of textbook H- and J-like excitonic interactions on the spectral features of the solid-state phase of these NFAs are expected to cancel out. This most probably leads to other factors (FE and CT states hybridization, environmental effects) being responsible for the peculiar electronic properties and photophysics of Y-family systems, as we have found here for the archetypic Y6. For the continued development of Y-series NFAs, we propose that the field should focus on further understanding the relationship between solid-state packing motifs, interaction networks, delocalization of exciton and charges and environmental effects. For example, by examining the impact of different chemical modifications to the molecular backbone of Y-series materials on the solid-state morphology, electronic properties, and excited state dynamics. Moving forward, explicit time-dependent propagation of coupled electron-nuclear motion through non-adiabatic molecular dynamic simulations [18,69,70] on realistic and more complex nano-scale microstructures could help us achieve this goal. By leveraging these structure-properties relationships, the optical and electronic properties of the NFA can be effectively controlled, potentially yielding new Y-series NFA materials that can drive power conversion efficiencies toward the elusive 20 % milestone.

Methods

Frenkel-Holstein Hamiltonian

To model optical properties and electronic states of tightly packed molecular aggregates with excited states of different characters, *i.e.*, FE and CT states, in the presence of local vibronic coupling to effective vibrational modes for hole, electron and excitonic states, we utilized the following Frenkel-Holstein-type Hamiltonian written as:

$$H = H_{\mathrm{FE}} + H_{\mathrm{CT}} + H_{\mathrm{FE-CT}} + H_{\mathrm{N}} + H_{\mathrm{FE-N}} + H_{\mathrm{CT-N}}. \tag{1}$$

H_{FE} represents the Frenkel-exciton block which describes the interactions between bound electron-hole pair residing on the same molecular site k. This can be written as:

$$H_{\mathrm{FE}} = \sum\nolimits_k \left(E^{(\mathrm{sol})}_{\mathrm{S_0 \to S_1}} + \Delta_{0-0}\right)|e_k\rangle\langle e_k| + \sum\nolimits_{k,l} V_{kl}|e_k\rangle\langle e_l|. \tag{2}$$

Here, the energy of a local Frenkel exciton ($|e_k\rangle$), in the crystal is given by $E^{(\mathrm{cry})}_{\mathrm{FE}} = E^{(\mathrm{sol})}_{\mathrm{S_0 \to S_1}} + \Delta_{0-0}$, where $E^{(\mathrm{sol})}_{\mathrm{S_0 \to S_1}}$ is the energy of the electronic transition in solution and Δ_{0-0} is the solution-to-crystal shift (which is a negative shift). The off-diagonal elements of this block are the excitonic couplings, V_{kl}, which describe the interactions between tightly bound electron-hole pair sitting either on molecules k or l and allow for excitation energy transfer between the two. These couplings are dominated by the Coulombic interaction between the transition densities of the two molecules. The magnitude of such an interaction scale as r^{-3}, where r is the intermolecular distance. We refer to Section S6 for a detailed explanation of how all these terms are calculated in practice using a combination of TDDFT and accurate BSE calculations.

The second term H_{CT} represents the charge transfer Hamiltonian which describe the interactions between charge transfer excitons. This is written as:

$$\begin{aligned}H_{\mathrm{CT}} = & \textstyle\sum_{k,s\neq 0}(E_{\mathrm{CT}}(r_s))|a_k, c_{k+s}\rangle\langle a_k, c_{k+s}| \\ & +\textstyle\sum_{k,s\neq 0,s'\neq 0} t_{\mathrm{h}}(s-s')|a_k, c_{k+s}\rangle\langle a_k, c_{k+s'}| \\ & +\textstyle\sum_{k,s\neq 0,s'\neq 0} t_{\mathrm{e}}(s-s')|a_{k+s}, c_k\rangle\langle a_{k+s'}, c_k|\end{aligned} \tag{3}$$

where the $|a_k, c_{k+s}\rangle$ denotes the charge transfer exciton where the cationic (anionic state) is located on the site k, while the hole (cationic state) is on molecule l located at distance s from the first molecule. The vectors s and s' denote the electron/hole separation (in lattice units) and are restricted to nonzero values. When $s = 0$ the electron and hole are located on the same molecule resulting in a FE excitation. $E_{\mathrm{CT}}\,(r_s)$ is the energy of the charge transfer state and it is determined in this work as described in Section S9. This term is defined by the Coulomb binding energy of hole and electron at a given distance r_s. $E_{\mathrm{CT}}\,(r_s)$ is therefore the smallest when the interacting hole and electron reside on the closest crystal pair and the energy difference of this (diabatic) state with respect to $E^{(\mathrm{cry})}_{\mathrm{S_0 \to S_1}}$ determines the energy offset (Δ_{offset}) between FE and CT states.

CT excitons couple to one another via electron and hole transfer integrals, t_{e} and t_{h}, respectively. The charge transfer integrals are a result of the interactions between either the HOMO orbitals or the LUMO orbitals of two interacting chromophores, and they are influenced by the extent of spatial overlap between them. Consequently, the coupling decreases exponentially as the distance between the chromophores increases, and it is typically noteworthy only for closely interacting molecules (*e.g.*, nearest neighbours). See Section S7 for details of the actual computation of these terms. The mixing between FE and CT excitons is given by the Hamiltonian block $H_{\mathrm{FE-CT}}$ which is written as:

$$\begin{aligned}H_{\mathrm{FE-CT}} = & \textstyle\sum_{k,s\neq 0} D_{\mathrm{h}}(s)|e_k\rangle\langle a_k, c_{k+s}| + h.c. \\ & +\textstyle\sum_{k,s\neq 0} D_{\mathrm{e}}(s)|e_k\rangle\langle a_{k+s}, c_k| + h.c.\end{aligned} \tag{4}$$

where $D_{\mathrm{e}}(s)$ and $D_{\mathrm{h}}(s)$ are the photoinduced electron and hole transfer interactions, respectively, which couple FE and CT states, and where h.c. stands for the Hermitian conjugate. This Hamiltonian block is crucial because it allows dark CT states to borrow oscillator strength from bright FE. This, in turn, significantly impacts the optical properties of the aggregate. It is worth noticing that as carefully described in Ref. [71], $D_{\mathrm{e}}(s)$ and $D_{\mathrm{h}}(s)$ are not strictly the same as t_{e} and t_{h}, since additional exchange-like terms appear in the expression of the former couplings. However, the leading contribution in the calculation of $D_{\mathrm{e}}(s)$ and $D_{\mathrm{h}}(s)$ is related to the one-electron terms (Fock matrix elements) involving the interaction of LUMO orbitals for the former and HOMO orbitals for the latter as it is the case for t_{e} and t_{h}. Consequently, these terms decay exponentially with the distance between donor and acceptor sites as well.

Nuclear degrees of freedoms are also accounted for in our Hamiltonian. The electronic excitations (*i.e.*, the formation of anionic, cationic and excitonic states) are characterized by a strong coupling with high-frequency vibrational modes (which are represented here by a single effective mode with effective energy $\hbar\omega_{\mathrm{eff}}$, to make the problem computationally feasible). This vibronic interaction is responsible for the pronounced vibronic progression observed in the spectra. H_{N} describes the nuclear energy and it is written as:

$$H_{\mathrm{N}} = \hbar\omega_{\mathrm{eff}} \textstyle\sum_k b^{\dagger}_k b_k \tag{5}$$

where $b^{\dagger}_k$ and b_k are the common creation and annihilation operators associated with a quantum harmonic oscillator. Here, we have assumed that both excited and ground states to have the same curvature and we have also omitted the zero-point energy, which is uniform for all molecules. This exclusion does not impact our findings since we are focusing on the energy differences between the eigenstates.

Finally, the coupling between electron and nuclei is given by $H_{\mathrm{FE-N}}$ and $H_{\mathrm{CT-N}}$ terms written as:

$$H_{\mathrm{FE-N}} = \hbar\omega_{\mathrm{eff}}\sqrt{S_{\mathrm{e}}} \textstyle\sum_k (b^{\dagger}_k + b_k + \sqrt{S_{\mathrm{e}}})|e_k\rangle\langle e_k| \tag{6}$$

and

$$\begin{aligned}H_{\mathrm{CT-N}} = & \hbar\omega_{\mathrm{eff}}\sqrt{S_{\mathrm{a}}}\textstyle\sum_{k,s\neq 0}(b^{\dagger}_k + b_k + \sqrt{S_{\mathrm{a}}})|a_k, c_{k+s}\rangle\langle a_k, c_{k+s}| \\ & + \hbar\omega_{\mathrm{eff}}\sqrt{S_{\mathrm{c}}}\textstyle\sum_{k,s\neq 0}(b^{\dagger}_{k+s} + b_{k+s} + \sqrt{S_{\mathrm{c}}})|a, c_{k+s}\rangle\langle a_k, c_{k+s}|\end{aligned} \tag{7}$$

where $S_{\mathrm{e,c,a}}$ are the Huang-Rhys factors of the excitonic, cationic and anionic states, respectively, related to the displacement ($d_{\mathrm{e,c,a}}$) of the excited state potential (*i.e.*, anionic, cationic or excitonic) with respect to the ground state. As described in Section S3, $S_{\mathrm{e,c,a}} = \frac{\lambda^{\mathrm{rel}}_{\mathrm{e,c,a}}}{\hbar\omega_{\mathrm{eff}}} = \frac{m\omega_{\mathrm{eff}} {d_{\mathrm{e,c,a}}}^2}{2\hbar}$. In Eq. (7) the first summation accounts for vibronic coupling to cationic states while the second term accounts for the vibronic coupling to anionic states.

The Hamiltonian matrix is expressed in a multi-particle basis set, which is commonly truncated to two particle states referred to as the two particle approximation (TPA), and numerically diagonalized [31,32]. Such a basis set has been extensively used by Spano et al. [31,32] to represent the low energy eigenstates of the Hamiltonian in the regimes of weak and intermediate electronic coupling. In this basis, the eigenstate j of the Hamiltonian can be written as:

$$\begin{aligned}|\Psi^{(j)}\rangle = & \sum_k \sum_{v^{\sim}=0}^{v_{\max}} c^{(j)}_{k,v^{\sim}} \left|e_k, \tilde{v}_k\right\rangle + \sum_k \sum_{l\neq k} \sum_{v^{\sim}=0}^{v_{\max}-1} \\ & \times \sum_{v=1}^{v_{\max}-v^{\sim}} c^{(j)}_{k,v^{\sim},l,v} |e_k, \tilde{v}_k; g_l, v_l\rangle + \sum_k \sum_{l\neq k} \sum_{v^{\sim+}=0}^{v_{\max}} \\ & \times \sum_{v^{\sim-}=0}^{v_{\max}} d^{(j)}_{k,v^{\sim-},l,v^{\sim+}} |a_k, \tilde{v}^{-}_k; c_l, \tilde{v}^{+}_l\rangle\end{aligned} \tag{8}$$

where the first two terms correspond to one- and two-particle FE excitations, respectively, with $\tilde{v}$ and v representing the vibrational energy levels in the shifted excited state potential and ground state potential respectively. While the last term introduces two-particle charge transfer states in which $\tilde{v}^{+}$, vibrational quanta reside on the cation and $\tilde{v}^{-}$ vibrational quanta reside on the anion. A detail description of the computation of the different parameters is provided in SI along with the related level of theory used for each parameter.

General simulation details

Electronic structure calculations have been performed for the triclinic Y6 unit cell reported by Xiao et al. [36] Due to the very large thermal ellipsoids of the published structure, bond lengths and angles of individual molecules have been optimized (as described in Section S1). Y6 alkyl side chains have been replaced by methyl groups in all TDDFT and many-body calculations.

The polarizable continuum model (PCM) has been used to describe Y6 in solution [24], using the geometries optimized in each specific solvent. Solid-state calculations considered electrostatic and dielectric embedding in the infinite bulk limit, described at the atomistic level [24,25]. The classical (MM) environment has been described with the induced-dipole model implemented in the MESCal code [29], parameterized with polarizability tensor and atomic charges (ESP scheme) computed with TDDFT. The classical dielectric response of alkyl side chains, not provided in the experimental crystal structure [36], has been modelled with a grid of polarizable points occupying the corresponding cavity and bearing the polarizability of the replaced alkyl chains. The static dielectric tensor of the Y6 triclinic unit cell, built as in Section S1, has been computed with a microelectrostatic (ME) model by applying a uniform electric field along the three Cartesian directions, as explained in Ref. [29] It has been previously shown that ME calculations, performed with the MESCal code, provide accurate values of the susceptibility tensor for crystal and molecular films. We refer the interested reader to Ref. [72].

The Frenkel-Holstein Hamiltonian in Eq. (1) has been constructed for Y6 crystal using a combination of embedded many-body GW/BSE/MM (for the site-energies) and TDDFT (for the electronic interactions) as described in the main text and further detailed below. The converged Hamiltonian is constructed for 3x3x3 cell size and using 3 vibrational quanta for all electronic excitations (FE and CT states). Periodic boundary conditions are taken into account using a minimum image convention for all the electronic interactions. Convergence with respect to different parameters used in the Hamiltonian is presented in Fig. S9.

Embedded many-body GW/BSE and time dependent density functional theory

Embedded many-body GW and BSE calculations have been performed with the FIESTA and beDeft codes [73,74]) adopting the formalism described in the original papers [24,25]. Kohn-Sham orbitals have been computed at the PBE0/6-311G(d) level of theory with the ORCA package [75]. Many-body calculations employed resolution-of-the-identity (RI-V) techniques [76], using the universal Weigend Coulomb fitting basis set [77]. Quasiparticle energies have been computed with a self-consistent scheme on eigenvalues (evGW), correcting one (two) occupied and unoccupied levels for a Y6 molecule (dimer). Neutral singlet excitations have been obtained at the full BSE level, using an active space constructed by occupied-virtual transitions between states within 15 eV from the corresponding band edge. Solid-state BSE/GW/MM calculations have been performed for the different QM/MM partitioning schemes, namely considering as QM region: (i) each of the two symmetry-unique Y6 molecules in the crystal (results in Tables S4 and S5; (ii) eight Y6 dimers chosen among the closest distance pairs (results in Table S7). The latter have been used to parameterize the model Hamiltonian for CT excited states energy of the crystal as explained in Section S9.

The electronic couplings, vibrational analysis and other parameters are computed using TDDFT. Specifically, we used an optimally-tuned (OT) range-separated hybrid (RSH) functional, unless stated otherwise. The tuning procedure adopted in this work with the LC-ωhPBE functional and the 6-311G(d,p) basis set is described in Section S2 and the OT ω value was found at 0.101 Bohr^{-1} for the Y6 molecule [78]. With such a level of theory, excitonic couplings are computed using the multi-state diabatization fragment excitation energy difference-fragment charge difference (MS-FED-FCD) approach [53,79,80]. The electronic charge transfer couplings were calculated instead with the projection operator diabatization approach (POD) [81–83]. Both these approaches are briefly described in Sections S6 and S7.

Optical steady-state absorption

The steady-state absorption spectra of Y6 in chloroform and toluene solution has been recorded using a high-performance quartz cuvette (Hellma Analytics). The absorption spectrum has been determined via a transmission measurement using an UV–Vis-NIR spectrometer (Agilent Technologies Cary 5000 Series). The concentration of Y6 has been determined by diluting the solution so that the signal was not saturated as well as invariant under consecutive dilutions.

The film spectra have been obtained using a combination of reflection-transmission measurements using an integrating sphere, and reverse transfer matrix modelling approach developed by Kerremans *et al.* to obtain the optical constants of the films [40]. Three separate films with different thicknesses have been fabricated from chloroform solvent. This was done by spin casting the material on borosilicate glass substrates at 2000 rpm. All films were annealed at 120 °C. The different thicknesses have been obtained by dissolving the Y6 in solutions with different concentrations. The processing parameters and sample thicknesses are listed in Table S8, and the reverse transfer matrix modelling described more in details in Section S12. Sample thicknesses have been measured using a profilometer (Bruker DekTakXT).

Transient absorption spectroscopy

TAS has been performed on either one of two experimental setups. The femtosecond TAS in the IR region (1200–1600 nm) has been performed on a setup powered using a commercially available Ti:sapphire amplifier (Spectra Physics Solstice Ace). The amplifier operates at 1 kHz and generates 100 fs pulses centred at 800 nm with an output of 7 W. A portion of the laser fundamental was used for sample excitation at 800 nm. The broadband infrared probe pulse used in the femtosecond TAS measurements is provided by a home built non-colinear optical parametric amplifier (NOPA). The probe pulses are collected with an InGaAs dual-line array detector (Hamamatsu G11608-512DA), driven and read out by a custom-built board from Stresing Entwicklungsbüro. The probe beam has been split into two identical beams by a 50/50 beamsplitter. This allowed for the use of a second reference beam which also passes through the sample but does not interact with the pump. The role of the reference was to correct for any shot-to-shot fluctuations in the probe that would otherwise greatly increase the structured noise in our experiments.

For the 500–950 nm continuous probe region TAS, a Yb amplifier (PHAROS, Light Conversion), operating at 38 kHz and generating 200 fs pulses centred at 1030 nm with an output of 14.5 W has been used. The ~200 fs pump pulse was provided by an optical parametric amplifier (Light Conversion ORPHEUS). The probe is provided by a white light supercontinuum generated in a YAG crystal from a small amount of the 1030 nm fundamental. After passing through the sample, the probe is imaged using a Si photodiode array (Hamamatsu S11490).

Magnetic resonance spectroscopies

Photoluminescence-detected magnetic resonance (PLDMR) and transient electron paramagnetic resonance (trEPR) experiments were carried out with a modified X-band spectrometer (Bruker E300) equipped with a continuous-flow helium cryostat (Oxford ESR 900) and a microwave cavity (Bruker ER4104OR, 9.43 GHz) with optical access. All measurements have been performed at T = 10 K.

For PLDMR, microwaves have been generated with a microwave signal generator (Anritsu MG3694C), amplified to 3 W (microsemi) and guided into the cavity. Optical irradiation has been performed with a 473 nm continuous wave laser (Cobolt). PL has been detected with a silicon photodiode (Hamamatsu S2281) on the opposite opening of the cavity, using a 561 nm longpass filter to reject the excitation light. The PL signal has been amplified by a current/voltage amplifier (Femto DHPCA-100) and recorded by lock-in detector (Ametek SR 7230), referenced by on–off-modulating the microwaves with 517 Hz.

For trEPR, pulsed optical excitation has been performed with a Nd:YAG laser (Continuum Minilite II) with 532 nm; pulse length of 5 ns; 15 Hz repetition rate; 2 mJ per pulse. Microwaves have been generated and detected with a microwave bridge (Bruker ER047MRP). Measurements have been performed with 20 dB attenuation (2 mW). A voltage amplifier (FEMTO DHPVA-200) and a digitizer card (GaGe Razor Express 1642 CompuScope) have been used for transient recording. The time resolution is limited to ~100 ns by the cavity Q factor of around 2800. By sweeping the magnetic field, two-dimensional data sets are recorded, where trEPR spectra are averaged from 0.5–1.5 μs after laser excitation.

Spectroelectrochemistry

For the spectroelectrochemical samples, a 16 mg/mL solution of Y6 dissolved in chloroform was prepared and then stirred overnight at 45 °C under an inert nitrogen atmosphere. ITO coated glass substrates were sonicated in deionized water, acetone, and then isopropyl alcohol for 10 min each, and then were plasma ashed with O_2 plasma for 10 min. The Y6 films were spin coated at 1500 rpm for 70 s and then annealed for 20 min at 100 °C and left to cool until they were below 60 °C.

Cyclic voltammetry was conducted using a three-electrode setup, with the Y6 film as the working electrode, a Pt wire counter electrode, and an oxidized Ag wire reference electrode. For the oxidation measurements, a 0.1 M TBAPF6 solution in MeCN was used as the electrolyte. A PalmSens4 was used to run the electrochemical measurement. The electrochemical setup was placed inside a quartz cuvette, and the Y6 film was aligned in the beam path of a Bruker VERTEX 70v FT-IR spectrometer fitted with a Bruker DigiTect Mid-Infrared deuterated L-alanine doped triglycine sulphate (DLaTGS) detector with a KBr window. Scans were taken with a resolution of 4 cm^{-1}, aperture size of 3.5 mm, and scanner velocity of 5 kHz using the NIR source of the spectrometer.

Raman and ATR-FTIR experiments

To perform Raman measurements, samples were prepared by drop-casting onto calcium fluoride substrates from the same 10 mg mL^{-1} precursor solution as was used for the spin-coated samples. Drop-casting was necessary in order to achieve sufficient film thickness to yield a good SNR; Raman-grade calcium fluoride substrates, with a single characteristic peak at 321 cm^{-1} were required in order to give a clean, unstructured background signal and hence reliable spectra. All spectra were measured on a Raman microscope (Horiba T64000) with 532 nm excitation. Wavenumber calibration was achieved by indexing the characteristic 520.7 cm^{-1} Raman peak of a crystalline silicon wafer.

To perform attenuated total reflectance (ATR-FTIR) measurements, samples were prepared by spin-coating onto borosilicate float-glass substrates as described above. ATR-FTIR spectra were measured on an FTIR spectrometer (Bruker VERTEX 70v with ATR attachment). Additional details on the specific experimental adjustments are given in Section S13.

Associated content

Supporting information. Y6 crystal structure, Tuning of the long-range corrected functional, Reorganization energies and Huang-Rhys factors, Absorption spectrum, Fitting of Y6 single molecule spectrum, Frenkel-Holstein Hamiltonian for aggregate systems, Calculation of photoinduced electronic couplings, Calculation of charge transfer integrals, Calculation of excitation energies, Calculation of charge transfer excitations, Calculation of the character of the excited states, Convergence Y6 solid-state spectrum, Experimental spectrum spectrum of Y6 thin-film, Raman and ATR-FTIR, Transient absorption spectroscopy of Y6 in dilute media, Transient absorption spectroscopy of Y6 in BHJ blends, Additional Transient Absorption spectroscopy data on Y6 films, Spectroelectrochemistry measurements, Magnetic Resonance Spectroscopies.

CRediT authorship contribution statement

Samuele Giannini: Writing – review & editing, Writing – original draft, Software, Methodology, Investigation, Data curation. **Daniel J.C. Sowood:** Investigation, Data curation. **Jesús Cerdá:** Software, Methodology. **Siebe Frederix:** Investigation, Data curation. **Jeannine Grüne:** Investigation, Data curation. **Giacomo Londi:** Investigation, Data curation. **Thomas Marsh:** Investigation. **Pratyush Ghosh:** Investigation. **Ivan Duchemin:** Methodology. **Neil C. Greenham:** Supervision. **Koen Vandewal:** Writing – review & editing, Supervision. **Gabriele D'Avino:** Writing – review & editing, Supervision, Methodology. **Alexander J. Gillett:** Writing – original draft, Supervision, Investigation, Funding acquisition, Conceptualization. **David Beljonne:** Writing – review & editing, Supervision, Project administration, Funding acquisition, Conceptualization.

Data availability

Data will be made available on request.

Declaration of competing interest

The authors declare that they have no known competing financial interests or personal relationships that could have appeared to influence the work reported in this paper.

Acknowledgements

S.G. would like to acknowledge Jochen Blumberger, Lorenzo Cupellini, Nicholas J. Hestand, Raja Ghosh and Frank C. Spano for useful discussions at the beginning of the project. We thank Yiwen Wang for providing the donor:Y6 films used in this study. Andreas Sperlich and Vladimir Dyakonov are acknowledged for valuable discussions on PLDMR measurements throughout this work. We thank Ian Jacobs for assistance with the ATR-FTIR measurements. The work in Mons has been funded by the Belgian National Fund for Scientific Research (FRS-FNRS) within the Consortium des Équipements de Calcul Intensif (CÉCI), under Grant 2.5020.11, and by the Walloon Region (ZENOBE Tier-1 supercomputer), under grant 1117545. S.G. is “Chargé de recherches FNRS”. D.B. is a FNRS research director. S.G. thanks also the support of ICSC-Centro Nazionale di Ricerca in High Performance Computing, Big Data and Quantum Computing, funded by European Union-NextGenerationEU-PNRR, Missione 4 Componente 2 Investimento 1.4. J. C. acknowledges to European Union for its Marie Curie Individual fellowship (HORIZON-MSCA-2022-PF-01-01, project no. 101106941). Work in Grenoble has been supported by the French “Agence Nationale de la Recherche”, project RAPTORS (ANR-21-CE24-0004-01) and used high-performance computing resources from GENCI-TGCC (grant no. 2022-A0130910016). A.J.G. thanks the Leverhulme Trust for an Early Career Fellowship (ECF-2022-445). D.J.C.S. and N.C.G. thank the EPSRC for support (grants EP/W017091/1 and EP/L01551X/2). J.G. acknowledges support by the Deutsche Forschungsgemeinschaft (DFG, German Research Foundation) within the Research Training School “Molecular biradicals: Structure, properties and reactivity” (GRK2112) and the Bavarian Ministry of the Environment and Consumer Protection, the Bavarian Network “Solar Technologies Go Hybrid”.

Appendix A. Supplementary material

Supplementary material to this article can be found online at https://doi.org/10.1016/j.mattod.2024.09.009.

References

[1] L. Zhu et al., Nat. Mater. 21 (2022) 656–663.
[2] Y. Cui et al., Adv. Mater. 33 (2021) 2102420.
[3] J. Yuan et al., Nat. Commun. 10 (2019) 570.
[4] J. Yuan et al., Joule 3 (2019) 1140–1151.
[5] J. Yuan, Y. Zou, Org. Electron. 102 (2022) 106436.
[6] B. Lu et al., Nano Sel. 2 (2021) 2029–2039.
[7] M.B. Price et al., Nat. Commun. 13 (2022) 2827.
[8] D. Kroh et al., Adv. Funct. Mater. 32 (2022) 2205711.
[9] R. Wang et al., J. Am. Chem. Soc. 142 (2020) 12751–12759.
[10] W. Liu, D. Andrienko, J. Chem. Phys. 158 (2023) 094108.
[11] E. Sağlamkaya et al., Mater. Horizons 10 (2023) 1825–1834.
[12] Y. Wang et al., Joule 7 (2023) 810–829.
[13] D. Padula, A. Landi, G. Prampolini, Energy Adv. 2 (2023) 1215–1224.
[14] G. Kupgan, X.K. Chen, J.L. Brédas, Mater. Today Adv. 11 (2021) 100154.
[15] G. Zhang et al., Nat. Commun. 11 (2020) 1–10.
[16] L. Zhu et al., Adv. Energy Mater. 10 (2020) 1904234.
[17] Y. Fu et al., Nat. Commun. 14 (2023) 1870.
[18] S. Giannini et al., Nat. Commun. 13 (2022) 2755.
[19] S. Giannini, J. Blumberger, Acc. Chem. Res. 55 (2022) 819–830.
[20] Y. Dong et al., Nat. Commun. 11 (2020) 4617.
[21] T.M. Clarke, J.R. Durrant, Chem. Rev. 110 (2010) 6736–6767.
[22] X.-K. Chen et al., Intermolecular CT excitons enable nanosecond excited-state lifetimes in NIR-absorbing non-fullerene acceptors for efficient organic solar cells (2023) 1–32.
[23] A. Classen et al., Nat. Energy 5 (2020) 711–719.
[24] I. Duchemin, D. Jacquemin, X. Blase, J. Chem. Phys. 144 (2016) .
[25] J. Li et al., J. Phys. Chem. Lett. 7 (2016) 2814–2820.
[26] X. Blase, I. Duchemin, D. Jacquemin, Chem. Soc. Rev. 47 (2018) 1022–1043.
[27] G. D’Avino et al., J. Phys. Condens. Matter 28 (2016) 433002.
[28] J. Li et al., Phys. Rev. B 97 (2018) 035108.
[29] G. D’Avino et al., J. Chem. Theory Comput. 10 (2014) 4959–4971.
[30] N.J. Hestand, F.C. Spano, Acc. Chem. Res. 50 (2017) 341–350.
[31] N.J. Hestand, F.C. Spano, Chem. Rev. 118 (2018) 7069–7163.
[32] F.C. Spano, Acc. Chem. Res. 43 (2010) 429–439.
[33] S. Kashani et al., Mater. Horizons 10 (2023) 443–453.
[34] X. Zou et al., Molecules 25 (2020) 4118.
[35] B. Boldrini et al., J. Phys. Chem. A 106 (2002) 6286–6294.
[36] C. Xiao et al., J. Mater. Chem. C 8 (2020) 5370–5374.
[37] F. Regnier et al., J. Mater. Chem. C 11 (2023) 7451–7461.
[38] W. Zhu et al., J. Am. Chem. Soc. 142 (2020) 14532–14547.
[39] Z. Bi et al., J. Mater. Chem. A 9 (2021) 16733–16742.
[40] R. Kerremans et al., Adv. Opt. Mater. 8 (2020) .
[41] P. Wan et al., J. Phys. Chem. Lett. 12 (2021) 10595–10602.
[42] X. Chang, M. Balooch Qarai, F.C. Spano, J. Phys. Chem. C 126 (2022) 18784–18795.
[43] N.J. Hestand et al., J. Am. Chem. Soc. 138 (2016) 11762–11774.
[44] H. Yamagata et al., J. Chem. Phys. 134 (2011) 204703.
[45] J. Cerezo, F. Santoro, J. Comput. Chem. 44 (2023) 626–643.
[46] F.C. Spano, J. Chem. Phys. 116 (2002) 5877–5891.
[47] F.C. Spano et al., J. Chem. Phys. 129 (2008) 1–14.
[48] J. Clark et al., Phys. Rev. Lett. 98 (2007) 206406.
[49] R. Ghosh, C.M. Pochas, F.C. Spano, J. Phys. Chem. C 120 (2016) 11394–11406.
[50] R. Ghosh et al., Chem. Mater. 31 (2019) 7033–7045.
[51] A. Dreuw, J.L. Weisman, M. Head-Gordon, J. Chem. Phys. 119 (2003) 2943–2946.
[52] Z.-Q. You, C.-P. Hsu, Int. J. Quantum Chem. 114 (2014) 102–115.
[53] L. Cupellini et al., Wires Comput. Mol. Sci. 9 (2019) 1–23.
[54] T. Li et al., JACS Au 1 (2021) 1733–1742.
[55] G.D. Scholes, Proc. R. Soc. A Math. Phys. Eng. Sci. 476 (2020) 20200278.
[56] S. Giannini et al., Nat. Mater. 22 (2023) 1361–1369.
[57] S. Mahadevan et al., Nat. Commun. 15 (2024) 2393.
[58] S. Karuthedath et al., Nat. Mater. 20 (2021) 378–384.
[59] W. Li et al., ACS Energy Lett. 3 (2018) 2159–2166.
[60] R.-Q. Png et al., Nat. Commun. 7 (2016) 11948.
[61] Y. Firdaus et al., Nat. Commun. 11 (2020) 5220.
[62] L.J.F. Hart et al., Adv. Energy Mater. 2301357 (2023) 1–13.
[63] S. Richert, C.E. Tait, C.R. Timmel, J. Magn. Reson. 280 (2017) 103–116.
[64] A. Privitera et al., Adv. Energy Mater. 12 (2022) .
[65] J. Grüne et al., Adv. Funct. Mater. 33 (2023) .
[66] J. De Ceuster et al., Phys. Rev. B - Condens. Matter Mater. Phys. 68 (2003) 1–9.
[67] F. Zhao et al., Sol. RRL 5 (2021) 1–10.
[68] P.J. Hore et al., Chem. Phys. Lett. 137 (1987) 495–500.
[69] W. Peng et al., J. Phys. Chem. Lett. 13 (2022) 7105–7112.
[70] S. Giannini et al., Nat. Commun. 10 (2019) 3843.
[71] X. Li et al., J. Chem. Theory Comput. 13 (2017) 3493–3504.
[72] G. D’Avino, D. Vanzo, Z.G. Soos, J. Chem. Phys. 144 (2016) .
[73] X. Blase, C. Attaccalite, V. Olevano, Phys. Rev. B 83 (2011) 115103.
[74] I. Duchemin, X. Blase, J. Chem. Theory Comput. 16 (2020) 1742–1756.
[75] F. Neese, Wiley Interdiscip. Rev. Comput. Mol. Sci. 2 (2012) 73–78.

[76] I. Duchemin, J. Li, X. Blase, J. Chem. Theory Comput. 13 (2017) 1199–1208.
[77] F. Weigend, Phys. Chem. Chem. Phys. 8 (2006) 1057–1065.
[78] Z. Zheng et al., J. Phys. Chem. Lett. 8 (2017) 3277–3283.
[79] M. Nottoli et al., Photosynth. Res. 137 (2018) 215–226.
[80] J. Tölle et al., J. Chem. Phys. 153 (2020) 184113.
[81] Z. Futera, J. Blumberger, J. Phys. Chem. C 121 (2017) 19677–19689.
[82] O.G. Ziogos et al., J. Chem. Phys. 155 (2021) 234115.
[83] I. Kondov et al., J. Phys. Chem. C 111 (2007) 11970–11981.
[84] S. Giannini, J. Cerdá, G. Prampolini, F. Santoro, D. Beljonne, J. Mater. Chem. C 12 (2024) 10009–10028.